Broadband dynamic rupture modeling with fractal fault roughness, frictional heterogeneity, viscoelasticity and topography: the 2016 Mw 6.2 Amatrice, Italy earthquake

Taufiqurrahman Taufiqurrahman[1], Alice-Agnes Gabriel[1], Thomas Ulrich[2], Lubica Valentova[3], and Frantisek Gallovič[4]

[1]Ludwig-Maximilians-Universität München
[2]Ludwig-Maximilians-Universität
[3]Charles University, Faculty of Mathematics and Physics, Dept. of Geophysics
[4]Charles University, Faculty of Mathematics and Physics, Department of Geophysics

November 21, 2022

Abstract

Advances in physics-based earthquake simulations, utilizing high-performance computing, have been exploited to better understand the generation and characteristics of the high-frequency seismic wavefield. However, direct comparison to ground motion observations of a specific earthquake is challenging. We here propose a new approach to simulate data-fused broadband ground motion synthetics using 3D dynamic rupture modeling of the 2016 Mw6.2 Amatrice, Italy earthquake. We augment a smooth, best-fitting model from Bayesian dynamic rupture source inversion of strong-motion data (<1 Hz) with fractal fault roughness, frictional heterogeneities, viscoelastic attenuation, and topography. The required consistency at long periods allows us to quantify the role of dynamic source heterogeneities, such as the 3D roughness drag, from observational broadband seismic waveforms. We demonstrate that 3D data-constrained fully dynamic rupture synthetics show good agreement with various observed ground-motion metrics up to ~5 Hz and are an important avenue towards non-ergodic, physics-based seismic hazard assessment.

Broadband dynamic rupture modeling with fractal fault roughness, frictional heterogeneity, viscoelasticity and topography: the 2016 Mw 6.2 Amatrice, Italy earthquake

T. Taufiqurrahman[1], A.-A. Gabriel[1], T. Ulrich[1], L. Valentová[2], F. Gallovič[2]

[1]Department of Earth and Environmental Sciences, Faculty of Geosciences, Ludwig Maximilian University, Munich, Germany

[2]Department of Geophysics, Faculty of Mathematics and Physics, Charles University, Prague, Czech Republic

Corresponding author:

Taufiq Taufiqurrahman (taufiqurrahman@outlook.de)

Alice-Agnes Gabriel (gabriel@geophysik.uni-muenchen.de)

Key Points:

- We propose a novel approach to design data-driven, 3D physics-based broadband dynamic rupture scenarios from Bayesian dynamic inversion
- Our synthetics fit observations in terms of velocity and accelerations waveforms, as well as Fourier-amplitude-spectra up to ~ 5 Hz
- Analyzing the role of earthquake modeling ingredients highlights the importance of dynamic source heterogeneity for broadband ground-motion

Abstract

Advances in physics-based earthquake simulations, utilizing high-performance computing, have been exploited to better understand the generation and characteristics of the high-frequency seismic wavefield. However, direct comparison to ground motion observations of a specific earthquake is challenging. We here propose a new approach to simulate data-fused broadband ground motion synthetics using 3D dynamic rupture modeling of the 2016 Mw6.2 Amatrice, Italy earthquake. We augment a smooth, best-fitting model from Bayesian dynamic rupture source inversion of strong-motion data (<1 Hz) with fractal fault roughness, frictional heterogeneities, viscoelastic attenuation, and topography. The required consistency to match long periods allows us to quantify the role of small-scale dynamic source heterogeneities, such as the 3D roughness drag, from observational broadband seismic waveforms. We demonstrate that 3D data-constrained fully dynamic rupture synthetics show good agreement with various observed ground-motion metrics up to ~5 Hz and are an important avenue towards non-ergodic, physics-based seismic hazard assessment.

Plain Language Summary

Models of earthquakes are used to better understand the origin and features of strong seismic shaking using supercomputers. But the connection of such computer simulations with actual measurements is complex. This study suggests a new way to use observations, computer models, and physics to model details of the damaging ground shaking recorded during the 2016 Amatrice, Italy, earthquake. We start from an earlier, relatively low-resolution earthquake model that matches seismograms at low periods (<0.5-1Hz), derived using many Monte Carlo simulations. We carefully enhance this earthquake model by adding roughness to the slipping fault, smaller-scale variations of the frictional resistance of this fault to earthquake slip, mountains and basins scattering the seismic waves, and the effects of anelastic damping of wave amplitudes while they propagate. We show that we now also match the seismic waves at frequencies up to 5 Hz, while not losing the good match at long periods. This result is important to better understand how hazardous earthquakes in specific regions may be. Our modeling indicates which ingredients are required in computer simulations to generate realistic ground motions for physics-based seismic hazard assessment.

1 Introduction

Simulations of broadband (> 1 Hz) ground motions are of great importance to seismologists and the earthquake engineering community. Despite the fact that we often lack detailed knowledge of the subsurface and earthquake source processes at small scales, it is essential to understand the generation and characteristics of the high-frequency seismic wavefield coinciding with most buildings' resonance frequencies. Broadband ground motions have been successfully simulated using hybrid techniques (e.g., Graves & Pitarka, 2010; Mai et al., 2010) that combine low-frequency deterministic ground motion synthetics with stochastically generated high-frequency components. However, hybrid synthetic waveforms lack deterministic information at higher frequencies and pose challenges in the realistic parameterization of wave propagation and earthquake rupture. Indeed, high-frequency radiation may arise, for instance, from acceleration and deceleration of the rupture front (Madariaga, 1977) caused by fault kinks, segmentation, or roughness (e.g., Shi & Day, 2013; Bydlon & Dunham, 2015), frictional or stress heterogeneities (e.g., Ripperger et al., 2008; Valentová et al., 2021) or from off-fault damage (e.g., Okubo et al., 2019; Yamashita, 2000). Additionally, the radiated wavefield is scattered by complex topography and structural heterogeneities (e.g., Imperatori & Mai, 2013; Takemura et al., 2015; Hartzell et al., 2016; Langer et al., 2019; Pitarka et al., 2021).

Recent advances in high-performance computing and dynamic earthquake rupture modeling allow deterministic 3D regional-scale broadband simulations to resolve frequencies up to 10 Hz (e.g., Heinecke et al., 2014; Rodgers et al., 2020; Savran & Olsen, 2020; Pitarka et al., 2021). Such simulations often assume a kinematic, thus predefined, finite earthquake source representation. In distinction, dynamic rupture models offer physically self-consistent descriptions of the earthquake rupture process. Generic dynamic rupture simulations across rough faults (both in 2D or 3D, e.g., Dunham et al., 2011; Shi & Day, 2013; Bydlon & Dunham, 2015; Withers et al., 2018; Bruhat et al., 2020) are characterized by highly complex rupture processes translating into ground motion synthetics that can match empirical ground-motion prediction equations (GMPEs).

In this study, we investigate 3D effects of fault roughness and regional topography on earthquake source dynamics and broadband ground motions by direct validation against observations. The August 24th, 2016, Mw 6.2 Amatrice earthquake (Chiaraluce et al., 2017; Michele et al., 2020) is the first in the Amatrice-Visso-Norcia earthquake sequence in the Central-Northern Apennine system of NW-SE aligned normal faults. It was the sequence's most destructive event, causing extensive damage to surrounding buildings and infrastructure (Michele et al., 2016). The earthquake was recorded by a remarkably dense network of strong ground motion instruments, including 20 near-source stations within a radius of 50 km from the earthquake epicenter (Figure 1, Table S1). The two closest stations, in Amatrice (AMT) and Norcia (NRC), are located only a few kilometers away from the fault.

The source process of the Amatrice event has been imaged using seismic data (Pizzi et al., 2017; Tinti et al., 2016), geodetic data (e.g., Cheloni et al., 2017; Walters et al., 2018), or both (Cirella et al., 2018; Kheirdast et al., 2021), suggesting pronounced source heterogeneities. However, kinematic finite-fault inversions are challenged by inherent non-uniqueness (Gallovič & Ampuero, 2015; Mai et al., 2016; Ragon et al., 2018; Shimizu et al., 2020; Tinti et al., 2021). Dynamic source inversions recovering friction parameters and the initial state of fault stress offer a data-driven source description compatible with earthquake physics (e.g., Peyrat & Olsen, 2004) but require a sufficiently simple dynamic rupture model to reduce the computational cost of the forward problem. A Bayesian dynamic inversion using the Parallel Tempering Monte Carlo algorithm (Sambridge, 2013; Gallovič et al., 2019a) was applied to the Amatrice earthquake, utilizing band-pass filtered (between 0.05 and 0.5-1 Hz) strong ground motion data by Gallovič et al. (2019b). Assuming a 1D medium with planar topography, the best-fitting model was used to predict ground motions up to higher frequencies than considered in the inversion (up to ~5 Hz). Yet this approach poorly matched the high-frequency content, presumably most sensitive to unresolvable small-scale features of the rupture process.

We here propose a new approach to simulate data-fused broadband ground motion synthetics using 3D dynamic rupture modeling. Our starting point is the best-fitting model from the Bayesian dynamic source inversion of the Amatrice earthquake (Figure 1b, hereafter named 'reference model'). We self-consistently augment this smooth reference model by adding fault roughness, small-scale frictional heterogeneities, viscoelastic attenuation, and topography yielding realistic high-frequency radiation without disrupting the large-scale characteristics of the reference model. The synthetic near-field ground motions show good agreement with various observed ground-motion metrics up to frequencies of ~5 Hz.

2 Ingredients for broadband dynamic rupture modeling

We build our model upon Bayesian dynamic rupture inversion of the 2016 Amatrice earthquake following the approach of Gallovič et al. (2019b) with the improved forward solver FD3D_TSN (Premus et al., 2020), which was verified in a suite of dynamic rupture benchmarks (Harris et al., 2018). The inversion is performed for a 30 km long and 14 km wide planar fault governed by a slip-weakening friction law (Ida, 1972; Palmer et al., 1973). The dynamic rupture slip rate functions along the fault are convolved with pre-calculated Green's functions representing impulse responses of the medium. In this step, the fault is dipping at 45°, embedded in the 1D velocity structure of Ameri et al. (2012) with a flat free surface. The dynamic models are characterized by three spatially heterogeneous parameters: (i) the initial shear stress along dip τ_i, (ii) the friction drop, μ_s-μ_d, with μ_s and μ_d the static and dynamic friction coefficient respectively, and (iii) the slip-weakening distance D_c. Yielding occurs when the shear stress τ reaches the fault strength $\tau_s=\mu_s\sigma_n$, where σ_n is assumed as linearly depth-dependent normal stress with a gradient of 8.52 MPa/km and a minimum value of 0.1 MPa. The initial along-strike shear stress $\tau_{strike0}$ is assumed to be zero. The dynamic friction coefficient μ_d is fixed to 0.4, and frictional cohesion of 0.5 MPa is assumed everywhere on the fault. The best-fitting model from the Bayesian inversion represents the reference model of this study. We then perform high-resolution enhanced 3D dynamic rupture simulations using the open-source software package SeisSol (https://github.com/SeisSol/SeisSol), resolving seismic wavefield up to 5 Hz (locally up to 10 Hz) within 50 km distance of the fault using an unstructured, statically adaptive mesh consisting of 80 million tetrahedral elements (Figure 1a, Text S1).

2.1 Fault roughness

The reference model's dynamic parameters are first bilinearly interpolated from their 1.75 km along-dip and 2.3 km along-strike reference resolution into a denser 25 m sampled grid (see Figure 2, column a). Next, we adapt the fault morphology to adhere to a band-limited self-similar (Hurst exponent H=1) fractal surface. The amplitude-to-wavelength ratio α of natural faults ranges between 10^{-4} and 10^{-2} (Power & Tullis, 1991), and we here use $\alpha=10^{-2}$ allowing comparability to earlier studies (Shi and Day, 2013; Fang & Dunham, 2013; Withers et al., 2018; Bruhat et al., 2020). The fractal surface wavelengths are band-limited between λ_{min} and λ_{max}. Choosing λ_{min}=200 m balances resolution requirements and computational cost for our setup and aligns with previous 3D fault roughness studies (Shi and Day, 2013; Fang & Dunham, 2013). Our choice of λ_{max}=2 km is motivated by the ~2 km spatial resolution of the dynamic parameters in the reference model.

2.2 3D roughness drag and heterogeneous initial stresses

Shear and normal stresses are dynamically perturbed by fault roughness during rupture propagation. The resulting 'roughness drag' (Dunham et al., 2011), an additional shear resistance to slip, was derived for a 1D rough fault in a 2D quasi-static boundary perturbation analysis by Fang and Dunham (2013) as

$$\tau_{drag}^{2D} = 8\,\pi^3\alpha^2\,G^*\Delta/\lambda_{min} \quad , \tag{1}$$

with Δ the fault slip, λ_{min} the minimum roughness wavelength, and $G^* = G/(1 - \nu)$ where G and ν are shear modulus and Poisson's ratio, respectively.

To preserve the overall characteristics of the reference scenario while incorporating fault roughness, we compensate the roughness drag in the initial loading by increasing the reference initial shear tractions as $\tau_{\mathrm{dip}} = \tau_{\mathrm{dip0}} + \tau_{\mathrm{drag}}^{\mathrm{3D}}$ and $\tau_{\mathrm{strike}} = \tau_{\mathrm{strike0}} + \tau_{\mathrm{drag}}^{\mathrm{3D}}$. We thus attempt to empirically approximate the roughness drag (following Dunham et al., 2011, but for the first time in 3D) as

$$\tau_{\mathrm{drag}}^{\mathrm{3D}} = C\, \tau_{\mathrm{drag}}^{\mathrm{2D}} \quad , \qquad (2)$$

where C is a dimensionless coefficient. In Text S2, we demonstrate that C depends on the minimum roughness wavelength λ_{min} and the number of elements n resolving λ_{min}, calculating $\tau_{\mathrm{drag}}^{\mathrm{2D}}$ using characteristics of the reference model slip distribution. For our choice of $n = 4$ elements to resolve $\lambda_{\mathrm{min}} = 200$ m, we obtain C of ~0.44. The average value of $\tau_{\mathrm{drag}}^{\mathrm{3D}}$ across the rupture area is ~1.4 MPa.

We account for the 3D roughness drag while preserving the smooth reference initial stress distribution by loading the rough fault with a heterogeneous regional stress tensor: we first adapt the smooth reference initial fault loading to balance roughness drag, then expose the now rough fault to the adapted loading (Text S3). As a result, the broadband model features roughness-induced small-scale fluctuations of the initial shear and normal tractions (Figure 2b), consisting of both releasing and restraining slopes that bring the fault closer and farther from failure, respectively (Figure S2).

2.3 Frictional heterogeneity

We perturb the smooth variation of the reference characteristic frictional slip weakening distance D_c^0, the spatially most variable dynamic parameter in the reference Bayesian dynamic inversion. The relative standard deviation of D_c is on the order of 50% (Gallovič et al., 2019b), highlighting its importance as a proxy for unaccounted geometrical and geological features. We use a band-limited fractal distribution. We prescribe $D_c = \max(0.14 \text{ m}, D_c^0 (1+\varepsilon))$, where 0.14 m is the minimum value of D_c^0, and ε follows a fractal distribution of amplitude-to-wavelength ratio $\alpha=10^{-4}$ generated from a different random seed than the one used for the fault roughness.

2.4 Topography and viscoelasticity

In our broadband dynamic rupture, the flat free surface used in the inversion is superseded by high-resolution topography data sampled to 150 m resolution (Farr et al., 2007). The modeled 3D domain spans 300 × 300 km horizontally and extends to a depth of 150 km to avoid any undesired reflections from the (imperfectly) absorbing boundaries. We incorporate the 1D velocity model, with V_p = 1.86V_s, and viscoelastic attenuation, with Q_p = 2Q_s, inferred by Ameri et al. (2012), see Table S2.

3 Broadband rupture dynamics and ground-motion validation

3.1 Rupture dynamics

We compare the broadband dynamic rupture model, incorporating fault roughness, small-scale D_c variation, and topography to the reference model with a planar fault, a flat free surface, and smoothly varying initial conditions, in terms of fault slip (Figures 1b, c), slip rate space-time evolution (Figures 2c, d), and moment rate release (Figure S3).

Figures 1b,c and 2c,d demonstrate similar large-scale slip evolution. The seismic moment of the broadband model is 2.8 x 10^{18} Nm, corresponding to M_w=6.24, which is comparable to the reference model with 2.6 x 10^{18} Nm seismic moment (M_w=6.20). We highlight that both models recover the remarkably weak and slow nucleation phase (Tinti et al., 2016; Gallovič et al., 2019b), as was also inferred for the Norcia earthquake (Tinti et al., 2021). The nucleation is followed by bilateral rupture, which is slower towards the NW than towards the SE in both models. At smaller scales, the broadband model features decoherence of rupture fronts (Shi &

Day, 2013). Locally fluctuating rupture speeds are due to acceleration and deceleration at releasing and restraining slopes, heterogeneous initial shear and normal traction, and D_c heterogeneity. Peak slip rates are increased by ~15% in the broadband model, while both models feature pulse-like ruptures, and rise time remains largely unaffected.

Comparisons of moment rate releases (Figure S3a), moment rate spectra (Figure S3b), and the second time-derivative of moment rate releases (Figure S3c) illustrate the effects of the fault roughness, heterogeneous loading, and D_c on the high-frequency rupture radiation. While the two distinct episodes of moment rate release are well recovered, its first peak is about 20% higher in the broadband model than the reference model (Figure S3a), reflecting the required increase in negative strength excess in the nucleation region.

3.2 Ground motions

Figure 3 compares the observed three-component velocity and acceleration waveforms recorded at the 20 strong-motion stations (Figure 1, Luzi et al., 2016) with synthetics from the broadband dynamic rupture model. The overall agreement in terms of waveform shape, duration, and amplitudes is good. Analogous plots for the reference model and the rough fault model without topography are shown in Figures S4 and S5, respectively.

To better appreciate the role of the fault roughness and topography, Figure 4 compares EW velocity and acceleration waveforms and Fourier Amplitude Spectra (FAS) of three models - the reference, the broadband rough fault model with topography, and the broadband rough fault model without topography - with observations at selected stations. All other components and stations are shown in Figures S6-S12. The synthetic waveforms of the broadband models match long-period data (0.05-0.5 Hz) equally well as the reference model. Contrarily, the reference model provides waveforms clearly depleted at high frequencies. A general trend is that both, fault roughness and topography, enhance waveforms at high frequencies, although not to the same extent at all stations. The increase in high-frequency content in the broadband waveforms without topography (green) is clearly limited in duration compared to the same model incorporating topography (red). High-frequency ground motions are amplified early-on by fault roughness, while topography-induced scattered waves prolong their duration. The combination of both effects is most pronounced in the central and SE part of the hanging wall region (see, e.g., stations PZI1, LSS, and SPD in Figure 4 and S7, or MSC, AMT, and ANT in Figure S6, S9, S10, and S12). At some stations (e.g., stations FOS and ASP), our broadband synthetic spectra are improved but yet underestimating the observed spectra at frequencies higher than 1 Hz.

Animations of the three components of the velocity wavefield for the reference and broadband models are shown in Movies S2-S7. They illustrate how seismic waves are both reflected and scattered upon propagating across sharp topographical features like mountains and hills, which explains the prolonged duration of the seismic signal for several receivers (e.g., stations LSS & SPD, Figure 4). Viscoelastic attenuation is important to capture the decay of seismic reverberations caused by topography scattering (Figure S13).

Figures S14 and S15 quantify the fit of the synthetic ground-motions of the broadband and reference models with observations using Goodness-of-fit (GOF) metrics (Olsen & Mayhew, 2010), including peak ground velocity and displacement, spectral acceleration, Fourier amplitude spectra, energy duration, and cumulative energy (Text S4). The broadband model with topography fits the observations better (GOF 45-65) than the reference model (GOF 35-55) and the broadband model without topography (GOF 40-60).

Figure S16 details the model bias and standard deviation over the 0.5-10 s period range, averaged over 20 stations used in this study. A near-zero model bias over a specific period suggests that our simulated ground motions match observations reasonably well. The reference model fits the observations only at periods longer than 2 s. Compared to the reference model, the fit of the broadband model without topography (Figure S16b) is improved (30-40% lower bias) at periods shorter than 2 s. The broadband model with topography shows an even better fit (40-50% lower bias than the reference model, Figure S16c), while both models preserve a perfect fit at periods longer than 2 s.

4 Discussion

Recorded broadband ground motions are widely used in earthquake engineering to inform the performance-based design of structures. Typically, generic strong-motion waveforms that fit specific ground motion metrics are selected from a strong-motion database for that purpose (Iervolino et al., 2010). Also, probabilistic seismic hazard analyses often rely on such so-called ergodic ground-motion models (GMMs, e.g., Petersen et al., 2019). Yet, these may not reflect the conditions of a specific region of interest. Regional synthetic broadband ground motions from 3D dynamic rupture inversions, which offer a physically consistent representation of earthquakes, can sample conditions that are not sufficiently constrained in empirical models towards the development of non-ergodic, physics-based GMMs (Graves et al., 2011; Frankel et al., 2018; Moschetti et al., 2017; Wirth et al., 2018; Withers et al., 2020). Our proposed broadband dynamic rupture models can be extended to account for other distinctive regional characteristics, such as a listric or segmented fault geometry, 3D velocity models including low velocity layers and basins, and fault zone plasticity (Roten et al., 2014). They may also inform PSHA-targeted kinematic rupture generators while inherently ensuring realistic scaling of earthquake characteristics (e.g., Savran & Olsen, 2020). Our models emphasize the need to include i) small-scale source characteristics to enhance the high-frequency source radiation during the rupture propagation, and ii) topography to increase the duration due to scattering. The duration of the latter effect is controlled by viscoelastic attenuation.

We carefully analyze the effects of adding roughness to a flat fault model. We counterbalance the consequent 3D roughness drag by increasing initial shear traction by $\tau_{\mathrm{drag}}{}^{\mathrm{3D}}$ (equation 2), calculated using the spatially variable slip amplitude Δ of the reference model. We explored an alternative model (not presented here), with constant Δ equal to the peak slip of the reference model (1.14 m). It generates a higher average $\tau_{\mathrm{drag}}{}^{\mathrm{3D}}$ of about 3.3 MPa (cf. 1.4 MPa, Section 2.2). It may be possible to identify alternative satisfying models based on constant Δ. Nevertheless, the here presented approach of constraining Δ by the spatially variable reference fault slip appears superior due to its simpler and better constrained parametrization.

Although our rough fault model with topography improves the waveform fit at high frequencies, some synthetics still underestimate the observations. More complete matching of the observed records may in future be enabled by: (i) considering smaller length scales (λ_{min}) of fault surface roughness, potentially further increasing high-frequency radiation at the cost of increased computational demands; (ii) incorporating larger-scale non-planar fault geometry such as a listric fault geometry which has been, for instance, suggested from satellite data (Tung and Masterlark, 2018) and which may modulate peak ground velocities as a consequence of curvature focusing effect (Passone and Mai, 2017); (iii) probing and quantifying the variability of the predicted shaking using alternative models from the Bayesian ensemble of the dynamic rupture inversion, and (iv) incorporating a more realistic Earth model to capture path and local site conditions, i.e., 3D velocity models, small-scale scattering media (Imperatori & Mai 2013, Bydlon & Dunham, 2015), site corrections (Rodgers et al., 2020) or non-linear soil effects (Roten et al., 2012). In particular, low-velocity sedimentary basins (Lee et al., 2009, Pischiutta et al., 2021) can significantly amplify the amplitude and duration of ground motions, which may lead to improved synthetics for stations with strong site-effects, e.g., CLF with site-class D (Table 1).

5 Conclusions

We present a novel approach for broadband dynamic rupture modeling constrained from low-frequency data towards generating physics-based, non-ergodic ground motion synthetics validated by observations. We generate broadband dynamic rupture models of the 2016 Mw 6.2 Amatrice earthquake by combining large-scale heterogeneous stress and frictional parameters, inferred from the best-fitting model of a Bayesian dynamic rupture inversion, with self-similar fault roughness and frictional (slip weakening distance) heterogeneity, topography, and viscoelastic seismic attenuation. We empirically quantify the 3D roughness drag by counterbalancing its effective dynamic stress perturbations. We obtain dynamic rupture scenarios that successfully reproduce the low-frequency (<1 Hz) source characteristics of the inverted dynamic model while simultaneously producing a realistic amount of high-frequency (up to ~5 Hz) radiation. The combined small-scale heterogeneities of the fault geometry, frictional strength, loading, and topography's prolonging coda effect yield comparable with observed strong motion records. Our work demonstrates 3D physics-based, broadband earthquake ground-motion simulations that are tightly constrained by data-driven dynamic earthquake source inversion and allows us to quantify the first-order role of dynamic source heterogeneities in the broadband seismic wavefield.

6 Data and Resources

We use the open-source software package SeisSol, available at https://github.com/SeisSol/SeisSol, branch 'Norcia_sequence', commit 181fc85d5c405a8c44fe21869fe736ab1f0206d5. Input files required to run broadband dynamic rupture simulations can be downloaded from https://zenodo.org/record/6386938. The reference dynamic rupture model parameters from the Bayesian inversion are available at https://github.com/fgallovic/fd3d_tsn_pt/tree/master/example/20160824-Amatrice. The topography data from the Shuttle Radar Topography Mission (SRTM) is retrieved using the SRTM.py python package (https://github.com/tkrajina/srtm.py). Observed strong ground motion waveforms recorded by the Rete Accelerometrica Nazionale (RAN) and the Rete Sismometrica Nazionale, operated by the Italian Department of Civil Protection (DPC) and the Istituto Nazionale di Geofisica e Vulcanologia (INGV) were downloaded from the Engineering Strong-Motion database (https://esm.mi.ingv.it/, Luzi et al., 2016; Lanzano et al., 2021).

Acknowledgments

The work presented in this paper was supported by funding from the German Research Foundation (DFG, GA 2465/2-1). TT, AAG and TU acknowledge additional funding from the European Union's Horizon 2020 research and innovation programme (TEAR ERC Starting grant no. 852992; ChEESE, grant agreement No. 823844), DFG (GA 2465/3-1), NSF (EAR-2121666) and SCEC (awards 20046, 21010). The authors acknowledge the Gauss Centre for Supercomputing e.V. (www.gauss-centre.eu, project pr63qo) for funding this project by providing computing time on the GCS Supercomputer SuperMUC-NG at Leibniz Supercomputing Centre (www.lrz.de), and King Abdullah University of Science and Technology

(KAUST) Supercomputing Laboratory (www.hpc.kaust.edu.sa) for computing time on Shaheen II (project k1343).

References

Ameri, G., Gallovič, F., & Pacor, F. (2012). Complexity of the Mw 6.3 2009 L'Aquila (central Italy) earthquake: 2. Broadband strong motion modeling. *Journal of Geophysical Research: Solid Earth*, *117*(B4). https://doi.org/10.1029/2011JB008729

Aochi, H., & Madariaga, R. (2003). The 1999 İzmit, Turkey, Earthquake: Nonplanar Fault Structure, Dynamic Rupture Process, and Strong Ground Motion. *Bulletin of the Seismological Society of America*, *93*(3), 1249–1266. https://doi.org/10.1785/0120020167

Bruhat, L., Klinger, Y., Vallage, A., & Dunham, E. M. (2020). Influence of fault roughness on surface displacement: From numerical simulations to coseismic slip distributions. *Geophysical Journal International*, *220*(3), 1857–1877. https://doi.org/10.1093/gji/ggz545

Bydlon, S. A., & Dunham, E. M. (2015). Rupture dynamics and ground motions from earthquakes in 2-D heterogeneous media. *Geophysical Research Letters*, *42*(6), 1701–1709. https://doi.org/10.1002/2014GL062982

Cheloni, D., De Novellis, V., Albano, M., Antonioli, A., Anzidei, M., Atzori, S., Avallone, A., Bignami, C., Bonano, M., Calcaterra, S., Castaldo, R., Casu, F., Cecere, G., De Luca, C., Devoti, R., Di Bucci, D., Esposito, A., Galvani, A., Gambino, P., … Doglioni, C. (2017). Geodetic model of the 2016 Central Italy earthquake sequence inferred from InSAR and GPS data. *Geophysical Research Letters*, *44*(13), 6778–6787. https://doi.org/10.1002/2017GL073580

Chiaraluce, L., Di Stefano, R., Tinti, E., Scognamiglio, L., Michele, M., Casarotti, E., Cattaneo, M., De Gori, P., Chiarabba, C., Monachesi, G., Lombardi, A., Valoroso, L., Latorre, D., & Marzorati, S. (2017). The 2016 Central Italy Seismic Sequence: A First Look at the Mainshocks, Aftershocks, and Source Models. *Seismological Research Letters*, *88*(3), 757–771. https://doi.org/10.1785/0220160221

Day, S. M., Dalguer, L. A., Lapusta, N., & Liu, Y. (2005). Comparison of finite difference and boundary integral solutions to three-dimensional spontaneous rupture. *Journal of Geophysical Research: Solid Earth*, *110*(B12). https://doi.org/10.1029/2005JB003813

Dumbser, M., & Käser, M. (2006). An arbitrary high-order discontinuous Galerkin method for elastic waves on unstructured meshes—II. The three-dimensional isotropic case. *Geophysical Journal International*, *167*(1), 319–336. https://doi.org/10.1111/j.1365-246X.2006.03120.x

Dunham, E. M., Belanger, D., Cong, L., & Kozdon, J. E. (2011). Earthquake Ruptures with Strongly Rate-Weakening Friction and Off-Fault Plasticity, Part 2: Nonplanar Faults. *Bulletin of the Seismological Society of America*, *101*(5), 2308–2322. https://doi.org/10.1785/0120100076

Duru, K., & Dunham, E. M. (2016). Dynamic earthquake rupture simulations on nonplanar faults embedded in 3D geometrically complex, heterogeneous elastic solids. *Journal of Computational Physics*, *305*, 185–207. https://doi.org/10.1016/j.jcp.2015.10.021

Eurocode 8, (EC8). (2004). *EN 1998-1, Design of structures for earthquake resistance, part 1: General rules, seismic actions and rules for buildings*. European Committee for Standardization (CEN).

Fang, Z., & Dunham, E. M. (2013). Additional shear resistance from fault roughness and stress levels on geometrically complex faults. *Journal of Geophysical Research: Solid Earth*, *118*(7), 3642–3654. https://doi.org/10.1002/jgrb.50262

Farr, T. G., Rosen, P. A., Caro, E., Crippen, R., Duren, R., Hensley, S., Kobrick, M., Paller, M., Rodriguez, E., Roth, L., Seal, D., Shaffer, S., Shimada, J., Umland, J., Werner, M., Oskin, M., Burbank, D., & Alsdorf, D. (2007). The Shuttle Radar Topography Mission. *Reviews of Geophysics*, *45*(2). https://doi.org/10.1029/2005RG000183

Frankel, A., Wirth, E., Marafi, N., Vidale, J., & Stephenson, W. (2018). Broadband Synthetic Seismograms for Magnitude 9 Earthquakes on the Cascadia Megathrust Based on 3D Simulations and Stochastic Synthetics, Part 1: Methodology and Overall Results. *Bulletin of the Seismological Society of America*, *108*(5A), 2347–2369. https://doi.org/10.1785/0120180034

Gallovič, F., & Ampuero, J.-P. (2015). A New Strategy to Compare Inverted Rupture Models Exploiting the Eigenstructure of the Inverse Problem. *Seismological Research Letters*, *86*(6), 1679–1689. https://doi.org/10.1785/0220150096

Gallovič, F., Valentová, Ľ., Ampuero, J.-P., & Gabriel, A.-A. (2019). Bayesian Dynamic Finite-Fault Inversion: 1. Method and Synthetic Test. *Journal of Geophysical Research: Solid Earth*, *124*(7), 6949–6969. https://doi.org/10.1029/2019JB017510

Graves, R., Jordan, T. H., Callaghan, S., Deelman, E., Field, E., Juve, G., Kesselman, C., Maechling, P., Mehta, G., Milner, K., Okaya, D., Small, P., & Vahi, K. (2011). CyberShake: A Physics-Based Seismic Hazard Model for Southern California. *Pure and Applied Geophysics*, *168*(3), 367–381. https://doi.org/10.1007/s00024-010-0161-6

Graves, R. W., & Pitarka, A. (2010). Broadband Ground-Motion Simulation Using a Hybrid Approach. *Bulletin of the Seismological Society of America*, *100*(5A), 2095–2123.

https://doi.org/10.1785/0120100057

Harris, R. A., Barall, M., Aagaard, B., Ma, S., Roten, D., Olsen, K., Duan, B., Liu, D., Luo, B., Bai, K., Ampuero, J., Kaneko, Y., Gabriel, A., Duru, K., Ulrich, T., Wollherr, S., Shi, Z., Dunham, E., Bydlon, S., … Dalguer, L. (2018). A Suite of Exercises for Verifying Dynamic Earthquake Rupture Codes. *Seismological Research Letters*, *89*(3), 1146–1162. https://doi.org/10.1785/0220170222

Hartzell, S., Ramírez-Guzmán, L., Meremonte, M., & Leeds, A. (2016). Ground Motion in the Presence of Complex Topography II: Earthquake Sources and 3D Simulations. *Bulletin of the Seismological Society of America*, *107*(1), 344–358. https://doi.org/10.1785/0120160159

Heinecke, A., Breuer, A., Rettenberger, S., Bader, M., Gabriel, Pelties, C., Bode, A., Barth, W., Liao, X., Vaidyanathan, K., Smelyanskiy, M., & Dubey, P. (2014). Petascale High Order Dynamic Rupture Earthquake Simulations on Heterogeneous Supercomputers. *SC '14: Proceedings of the International Conference for High Performance Computing, Networking, Storage and Analysis*, 3–14. https://doi.org/10.1109/SC.2014.6

Ida, Y. (1972). Cohesive force across the tip of a longitudinal-shear crack and Griffith's specific surface energy. *Journal of Geophysical Research (1896-1977)*, *77*(20), 3796–3805. https://doi.org/10.1029/JB077i020p03796

Iervolino, I., Galasso, C., & Cosenza, E. (2010). REXEL: computer aided record selection for code-based seismic structural analysis. *Bulletin of Earthquake Engineering*, *8*(2), 339–362. https://doi.org/10.1007/s10518-009-9146-1

Imperatori, W., & Mai, P. M. (2013). Broad-band near-field ground motion simulations in 3-dimensional scattering media. *Geophysical Journal International*, *192*(2), 725–744.

https://doi.org/10.1093/gji/ggs041

Käser, M., Hermann, V., & Puente, J. de la. (2008). Quantitative accuracy analysis of the discontinuous Galerkin method for seismic wave propagation. *Geophysical Journal International*, *173*(3), 990–999. https://doi.org/10.1111/j.1365-246X.2008.03781.x

Kheirdast, N., Ansari, A., & Custódio, S. (2021). Neuro-Fuzzy Kinematic Finite-Fault Inversion: 2. Application to the Mw6.2, August/24/2016, Amatrice Earthquake. *Journal of Geophysical Research: Solid Earth*, *126*(8), e2020JB020773. https://doi.org/10.1029/2020JB020773

Konno, K., & Ohmachi, T. (1998). Ground-motion characteristics estimated from spectral ratio between horizontal and vertical components of microtremor. *Bulletin of the Seismological Society of America*, *88*(1), 228–241.

Langer, L., Gharti, H. N., & Tromp, J. (2019). Impact of topography and three-dimensional heterogeneity on coseismic deformation. *Geophysical Journal International*, *217*(2), 866–878. https://doi.org/10.1093/gji/ggz060

Lanzano, G., Luzi, L., Cauzzi, C., Bienkowski, J., Bindi, D., Clinton, J., Cocco, M., D'Amico, M., Douglas, J., Faenza, L., Felicetta, C., Gallovic, F., Giardini, D., Ktenidou, O., Lauciani, V., Manakou, M., Marmureanu, A., Maufroy, E., Michelini, A., … Theodoulidis, N. (2021). Accessing European Strong-Motion Data: An Update on ORFEUS Coordinated Services. *Seismological Research Letters*, *92*(3), 1642–1658. https://doi.org/10.1785/0220200398

Lee, S.-J., Komatitsch, D., Huang, B.-S., & Tromp, J. (2009). Effects of Topography on Seismic-Wave Propagation: An Example from Northern Taiwan. *Bulletin of the Seismological Society of America*, *99*(1), 314–325. https://doi.org/10.1785/0120080020

Luzi, L., Puglia, R., Russo, E., D'Amico, M., Felicetta, C., Pacor, F., Lanzano, G., Çeken, U., Clinton, J., Costa, G., Duni, L., Farzanegan, E., Gueguen, P., Ionescu, C., Kalogeras, I., Özener, H., Pesaresi, D., Sleeman, R., Strollo, A., & Zare, M. (2016). The Engineering Strong-Motion Database: A Platform to Access Pan-European Accelerometric Data. *Seismological Research Letters*, *87*(4), 987–997. https://doi.org/10.1785/0220150278

Madariaga, R. (1977). High-frequency radiation from crack (stress drop) models of earthquake faulting. *Geophysical Journal International*, *51*(3), 625–651. https://doi.org/10.1111/j.1365-246X.1977.tb04211.x

Mai, P. M., Imperatori, W., & Olsen, K. B. (2010). Hybrid Broadband Ground-Motion Simulations: Combining Long-Period Deterministic Synthetics with High-Frequency Multiple S-to-S BackscatteringHybrid Broadband Ground-Motion Simulations: Combining Deterministic Synthetics with Backscattering. *Bulletin of the Seismological Society of America*, *100*(5A), 2124–2142. https://doi.org/10.1785/0120080194

Mai, P. M., Schorlemmer, D., Page, M., Ampuero, J., Asano, K., Causse, M., Custodio, S., Fan, W., Festa, G., Galis, M., Gallovic, F., Imperatori, W., Käser, M., Malytskyy, D., Okuwaki, R., Pollitz, F., Passone, L., Razafindrakoto, H. N. T., Sekiguchi, H., … Zielke, O. (2016). The Earthquake-Source Inversion Validation (SIV) Project. *Seismological Research Letters*, *87*(3), 690–708. https://doi.org/10.1785/0220150231

Michele, M., Chiaraluce, L., Di Stefano, R., & Waldhauser, F. (2020). Fine-Scale Structure of the 2016–2017 Central Italy Seismic Sequence From Data Recorded at the Italian National Network. *Journal of Geophysical Research: Solid Earth*, *125*(4), e2019JB018440. https://doi.org/10.1029/2019JB018440

Michele, M., Di Stefano, R., Chiaraluce, L., Cattaneo, M., De Gori, P., Monachesi, G., Latorre, D., Marzorati, S., Valoroso, L., Ladina, C., Chiarabba, C., Lauciani, V., & Fares, M. (2016). The Amatrice 2016 seismic sequence: A preliminary look at the mainshock and aftershocks distribution. *Annals of Geophysics; Vol 59, Fast Track (2016)*, *59*.

Moschetti, M. P., Hartzell, S., Ramírez-Guzmán, L., Frankel, A. D., Angster, S. J., & Stephenson, W. J. (2017). 3D Ground□Motion Simulations of Mw 7 Earthquakes on the Salt Lake City Segment of the Wasatch Fault Zone: Variability of Long-Period (T≥1 s) Ground Motions and Sensitivity to Kinematic Rupture Parameters. *Bulletin of the Seismological Society of America*, *107*(4), 1704–1723. https://doi.org/10.1785/0120160307

Okubo, K., Bhat, H. S., Rougier, E., Marty, S., Schubnel, A., Lei, Z., Knight, E. E., & Klinger, Y. (2019). Dynamics, Radiation, and Overall Energy Budget of Earthquake Rupture With Coseismic Off-Fault Damage. *Journal of Geophysical Research: Solid Earth*, *124*(11), 11771–11801. https://doi.org/10.1029/2019JB017304

Olsen, K. B., & Mayhew, J. E. (2010). Goodness-of-fit Criteria for Broadband Synthetic Seismograms, with Application to the 2008 Mw 5.4 Chino Hills, California, Earthquake. *Seismological Research Letters*, *81*(5), 715–723. https://doi.org/10.1785/gssrl.81.5.715

Palmer, A. C., Rice, J. R., & Hill, R. (1973). The growth of slip surfaces in the progressive failure of over-consolidated clay. *Proceedings of the Royal Society of London. A. Mathematical and Physical Sciences*, *332*(1591), 527–548. https://doi.org/10.1098/rspa.1973.0040

Passone, L., & Mai, P. M. (2017). Kinematic Earthquake Ground-Motion Simulations on Listric Normal Faults. *Bulletin of the Seismological Society of America*, *107*(6), 2980–2993. https://doi.org/10.1785/0120170111

Pelties, C., de la Puente, J., Ampuero, J.-P., Brietzke, G. B., & Käser, M. (2012). Three-dimensional dynamic rupture simulation with a high-order discontinuous Galerkin method on unstructured tetrahedral meshes. *Journal of Geophysical Research: Solid Earth*, *117*(B2). https://doi.org/10.1029/2011JB008857

Pelties, C., Gabriel, A.-A., & Ampuero, J.-P. (2014). Verification of an ADER-DG method for complex dynamic rupture problems. *Geoscientific Model Development*, *7*(3), 847–866. https://doi.org/10.5194/gmd-7-847-2014

Petersen, M. D., Shumway, A. M., Powers, P. M., Mueller, C. S., Moschetti, M. P., Frankel, A. D., Rezaeian, S., McNamara, D. E., Luco, N., Boyd, O. S., Rukstales, K. S., Jaiswal, K. S., Thompson, E. M., Hoover, S. M., Clayton, B. S., Field, E. H., & Zeng, Y. (2019). The 2018 update of the US National Seismic Hazard Model: Overview of model and implications. *Earthquake Spectra*, *36*(1), 5–41. https://doi.org/10.1177/8755293019878199

Peyrat, S., & Olsen, K. B. (2004). Nonlinear dynamic rupture inversion of the 2000 Western Tottori, Japan, earthquake. *Geophysical Research Letters*, *31*(5). https://doi.org/10.1029/2003GL019058

Pischiutta, M., Akinci, A., Tinti, E., & Herrero, A. (2021). Broad-band ground-motion simulation of 2016 Amatrice earthquake, Central Italy. *Geophysical Journal International*, *224*(3), 1753–1779. https://doi.org/10.1093/gji/ggaa412

Pitarka, A., Akinci, A., De Gori, P., & Buttinelli, M. (2021). Deterministic 3D Ground-Motion Simulations (0–5 Hz) and Surface Topography Effects of the 30 October 2016 Mw 6.5 Norcia, Italy, Earthquake. *Bulletin of the Seismological Society of America*. https://doi.org/10.1785/0120210133

Pizzi, A., Di Domenica, A., Gallovič, F., Luzi, L., & Puglia, R. (2017). Fault Segmentation as Constraint to the Occurrence of the Main Shocks of the 2016 Central Italy Seismic Sequence. *Tectonics*, *36*(11), 2370–2387. https://doi.org/10.1002/2017TC004652

Premus, J., Gallovič, F., Hanyk, L., & Gabriel, A. (2020). FD3D_TSN: A Fast and Simple Code for Dynamic Rupture Simulations with GPU Acceleration. *Seismological Research Letters*, *91*(5), 2881–2889. https://doi.org/10.1785/0220190374

Ragon, T., Sladen, A., & Simons, M. (2018). Accounting for uncertain fault geometry in earthquake source inversions – I: theory and simplified application. *Geophysical Journal International*, *214*(2), 1174–1190. https://doi.org/10.1093/gji/ggy187

Ripperger, J., Mai, P. M., & Ampuero, J.-P. (2008). Variability of Near-Field Ground Motion from Dynamic Earthquake Rupture Simulations. *Bulletin of the Seismological Society of America*, *98*(3), 1207–1228. https://doi.org/10.1785/0120070076

Rodgers, A. J., Pitarka, A., Pankajakshan, R., Sjögreen, B., & Petersson, N. A. (2020). Regional-Scale 3D Ground-Motion Simulations of Mw 7 Earthquakes on the Hayward Fault, Northern California Resolving Frequencies 0–10 Hz and Including Site-Response Corrections. *Bulletin of the Seismological Society of America*. https://doi.org/10.1785/0120200147

Roten, D., Olsen, K. B., Day, S. M., Cui, Y., & Fäh, D. (2014). Expected seismic shaking in Los Angeles reduced by San Andreas fault zone plasticity. *Geophysical Research Letters*, *41*(8), 2769–2777. https://doi.org/10.1002/2014GL059411

Roten, D., Olsen, K. B., & Pechmann, J. C. (2012). 3D Simulations of M 7 Earthquakes on the Wasatch Fault, Utah, Part II: Broadband (0–10 Hz) Ground Motions and Nonlinear Soil Behavior. *Bulletin of the Seismological Society of America*, *102*(5), 2008–2030.

https://doi.org/10.1785/0120110286

Sambridge, M. (2013). A Parallel Tempering algorithm for probabilistic sampling and multimodal optimization. *Geophysical Journal International*, *196*(1), 357–374. https://doi.org/10.1093/gji/ggt342

Savran, W. H., & Olsen, K. B. (2020). Kinematic Rupture Generator Based on 3-D Spontaneous Rupture Simulations Along Geometrically Rough Faults. *Journal of Geophysical Research: Solid Earth*, *125*(10), e2020JB019464. https://doi.org/10.1029/2020JB019464

Scognamiglio, L., Tinti, E., Casarotti, E., Pucci, S., Villani, F., Cocco, M., Magnoni, F., Michelini, A., & Dreger, D. (2018). Complex Fault Geometry and Rupture Dynamics of the MW 6.5, 30 October 2016, Central Italy Earthquake. *Journal of Geophysical Research: Solid Earth*, *123*(4), 2943–2964. https://doi.org/10.1002/2018JB015603

Shi, Z., & Day, S. M. (2013). Rupture dynamics and ground motion from 3-D rough-fault simulations. *Journal of Geophysical Research: Solid Earth*, *118*(3), 1122–1141. https://doi.org/10.1002/jgrb.50094

Shimizu, K., Yagi, Y., Okuwaki, R., & Fukahata, Y. (2020). Development of an inversion method to extract information on fault geometry from teleseismic data. *Geophysical Journal International*, *220*(2), 1055–1065. https://doi.org/10.1093/gji/ggz496

Simmetrix Inc. (2017). *SimModeler: Simulation Modeling Suite 11.0 Documentation*. www.simmetrix.org

Takemura, S., Furumura, T., & Maeda, T. (2015). Scattering of high-frequency seismic waves caused by irregular surface topography and small-scale velocity inhomogeneity. *Geophysical Journal International*, *201*(1), 459–474. https://doi.org/10.1093/gji/ggv038

Tinti, E., Casarotti, E., Ulrich, T., Taufiqurrahman, T., Li, D., & Gabriel, A.-A. (2021).

Constraining families of dynamic models using geological, geodetic and strong ground motion data: The Mw 6.5, October 30th, 2016, Norcia earthquake, Italy. *Earth and Planetary Science Letters*, *576*, 117237. https://doi.org/10.1016/j.epsl.2021.117237

Tinti, E., Scognamiglio, L., Michelini, A., & Cocco, M. (2016). Slip heterogeneity and directivity of the ML 6.0, 2016, Amatrice earthquake estimated with rapid finite-fault inversion. *Geophysical Research Letters*, *43*(20), 10,745-10,752. https://doi.org/10.1002/2016GL071263

Tung, S., & Masterlark, T. (2018). Resolving Source Geometry of the 24 August 2016 Amatrice, Central Italy, Earthquake from InSAR Data and 3D Finite-Element Modeling. *Bulletin of the Seismological Society of America*, *108*(2), 553–572. https://doi.org/10.1785/0120170139

Valentová, Ľ., Gallovič, F., & Hok, S. (2021). Near-Source Ground Motions and Their Variability Derived from Dynamic Rupture Simulations Constrained by NGA-West2 GMPEs. *Bulletin of the Seismological Society of America*, *111*(5), 2559–2573. https://doi.org/10.1785/0120210073

Walters, R. J., Gregory, L. C., Wedmore, L. N. J., Craig, T. J., McCaffrey, K., Wilkinson, M., Chen, J., Li, Z., Elliott, J. R., Goodall, H., Iezzi, F., Livio, F., Michetti, A. M., Roberts, G., & Vittori, E. (2018). Dual control of fault intersections on stop-start rupture in the 2016 Central Italy seismic sequence. *Earth and Planetary Science Letters*, *500*, 1–14. https://doi.org/10.1016/j.epsl.2018.07.043

Wirth, E. A., Frankel, A. D., Marafi, N., Vidale, J. E., & Stephenson, W. J. (2018). Broadband Synthetic Seismograms for Magnitude 9 Earthquakes on the Cascadia Megathrust Based on 3D Simulations and Stochastic Synthetics, Part 2: Rupture Parameters and Variability.

Bulletin of the Seismological Society of America, *108*(5A), 2370–2388. https://doi.org/10.1785/0120180029

Withers, K. B., Moschetti, M. P., & Thompson, E. M. (2020). A Machine Learning Approach to Developing Ground Motion Models From Simulated Ground Motions. *Geophysical Research Letters*, *47*(6), e2019GL086690. https://doi.org/10.1029/2019GL086690

Withers, K. B., Olsen, K. B., Day, S. M., & Shi, Z. (2018). Ground Motion and Intraevent Variability from 3D Deterministic Broadband (0–7.5 Hz) Simulations along a Nonplanar Strike-Slip Fault. *Bulletin of the Seismological Society of America*, *109*(1), 229–250. https://doi.org/10.1785/0120180006

Wollherr, S., Gabriel, A.-A., & Uphoff, C. (2018). Off-fault plasticity in three-dimensional dynamic rupture simulations using a modal Discontinuous Galerkin method on unstructured meshes: Implementation, verification and application. *Geophysical Journal International*, *214*(3), 1556–1584. https://doi.org/10.1093/gji/ggy213

Yamashita, T. (2000). Generation of microcracks by dynamic shear rupture and its effects on rupture growth and elastic wave radiation. *Geophysical Journal International*, *143*(2), 395–406. https://doi.org/10.1046/j.1365-246X.2000.01238.x

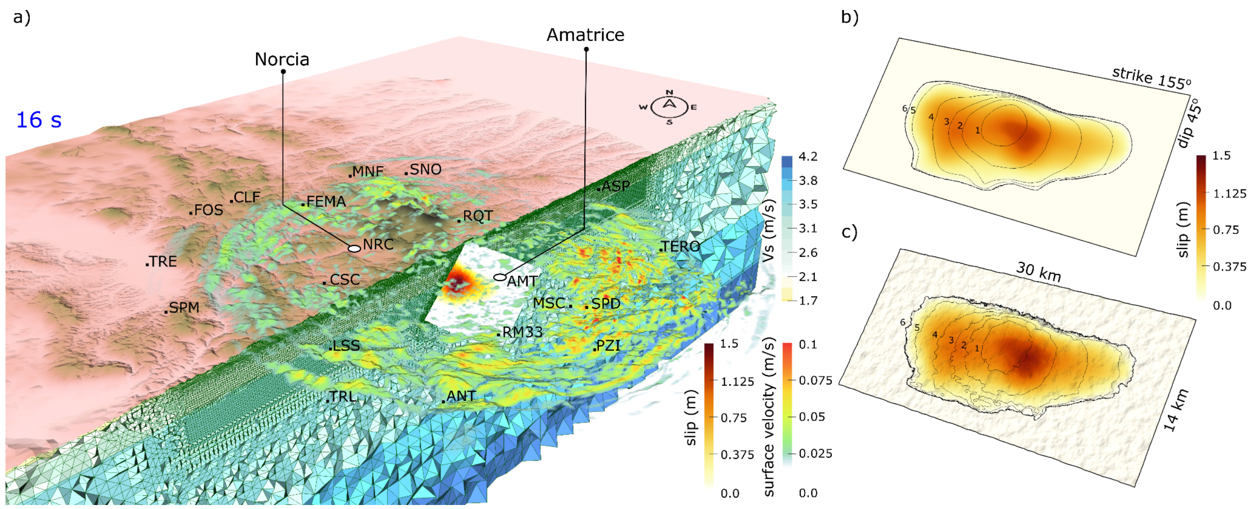

Figure 1. (a) Three-dimensional dynamic rupture model setup of the 2016 Mw 6.2 Amatrice, Central Italy, earthquake. Snapshot of the absolute surface velocity at a simulation time of 16 seconds. The model is discretized by an unstructured tetrahedral mesh refined in the vicinity of the fault and the high-resolution topography. Twenty strong-motion stations used in this study are marked in black (see Table S1). Mesh elements are colored by shear wave velocity (Vs). (b) and (c) Fault slip for the smooth Bayesian dynamic source inversion reference model (b) and the broadband dynamic rupture model (c). Black curves represent rupture front contours every 1 s.

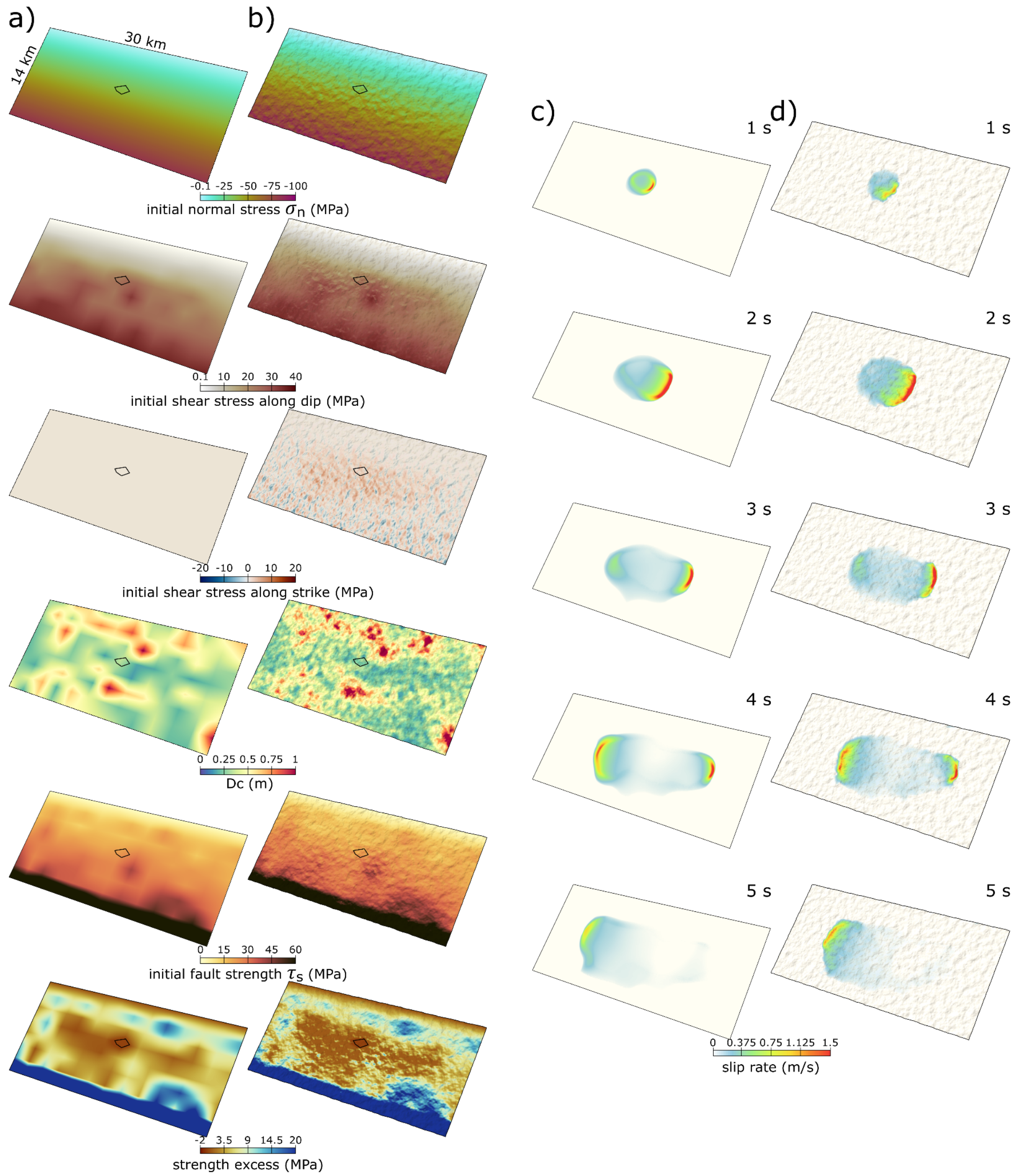

Figure 2. (a) and (b) Comparison of dynamic parameters used in the reference model (a), and the broadband rough fault model (b). Fractal heterogeneity is also added to the distribution of slip weakening distance (D_c). The black contour marks the nucleating negative strength excess area. (c) and (d) Dynamic rupture propagation in the reference (c) and broadband (d) rough fault models of the Amatrice earthquake. Snapshots of the absolute fault slip rates illustrate the similar space-time evolution in both models.

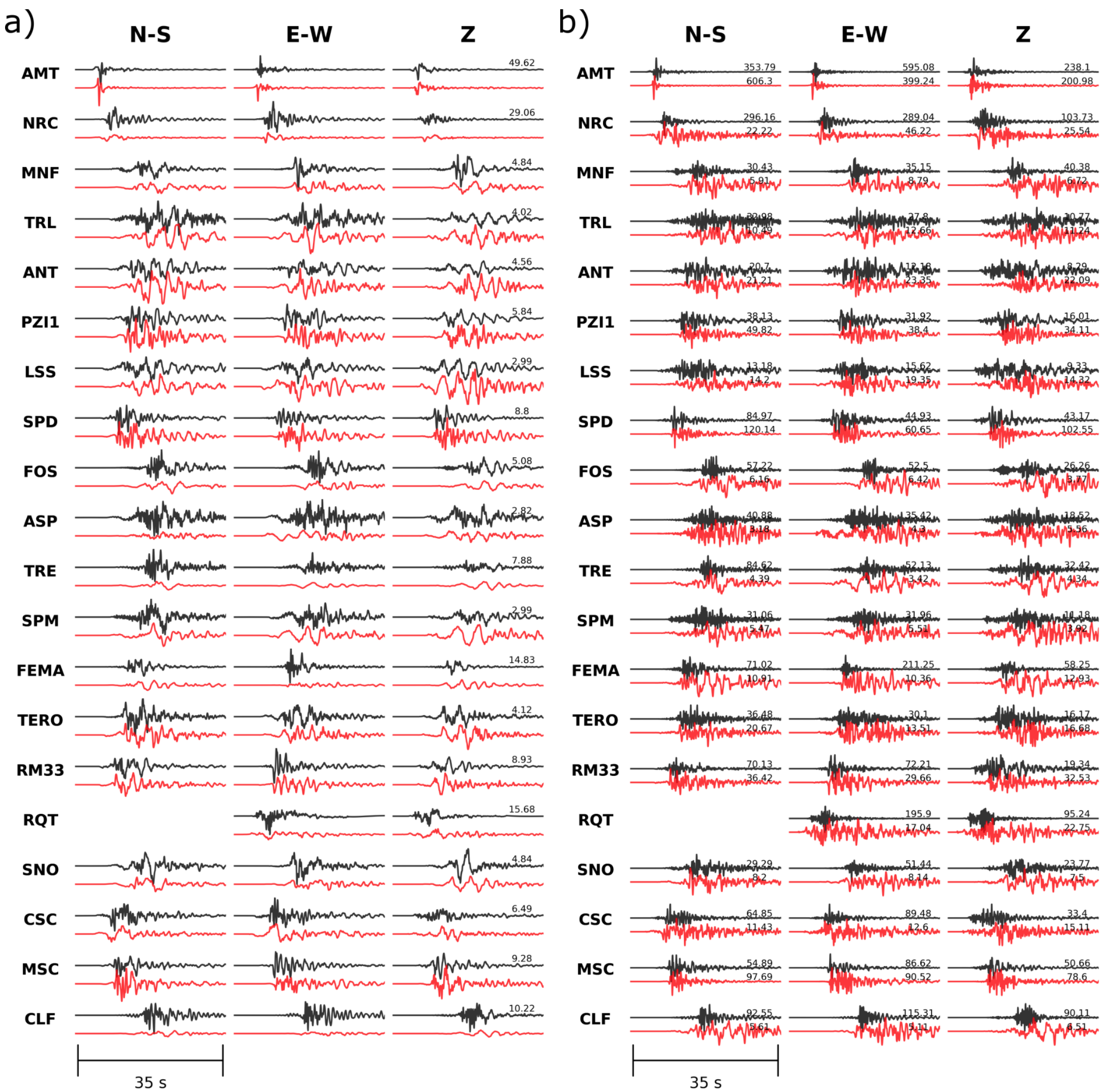

Figure 3. Comparison of observed (black) and simulated (red) components (NS, EW, and Z) of (a) ground velocity (in cm/s) and (b) acceleration (in cm/s^2) band-pass filtered between 0.05 and 5 Hz for all 20 stations (Figure 1). Synthetics are from the broadband dynamic rupture scenario incorporating fault roughness, D_c heterogeneity, and topography. Both observed and synthetic waveforms are scaled by their maximum value, which is indicated on the right-hand side of each plot. Velocity waveforms are scaled by the maximum value of the observed records at each station, while acceleration waveforms are scaled component-wise.

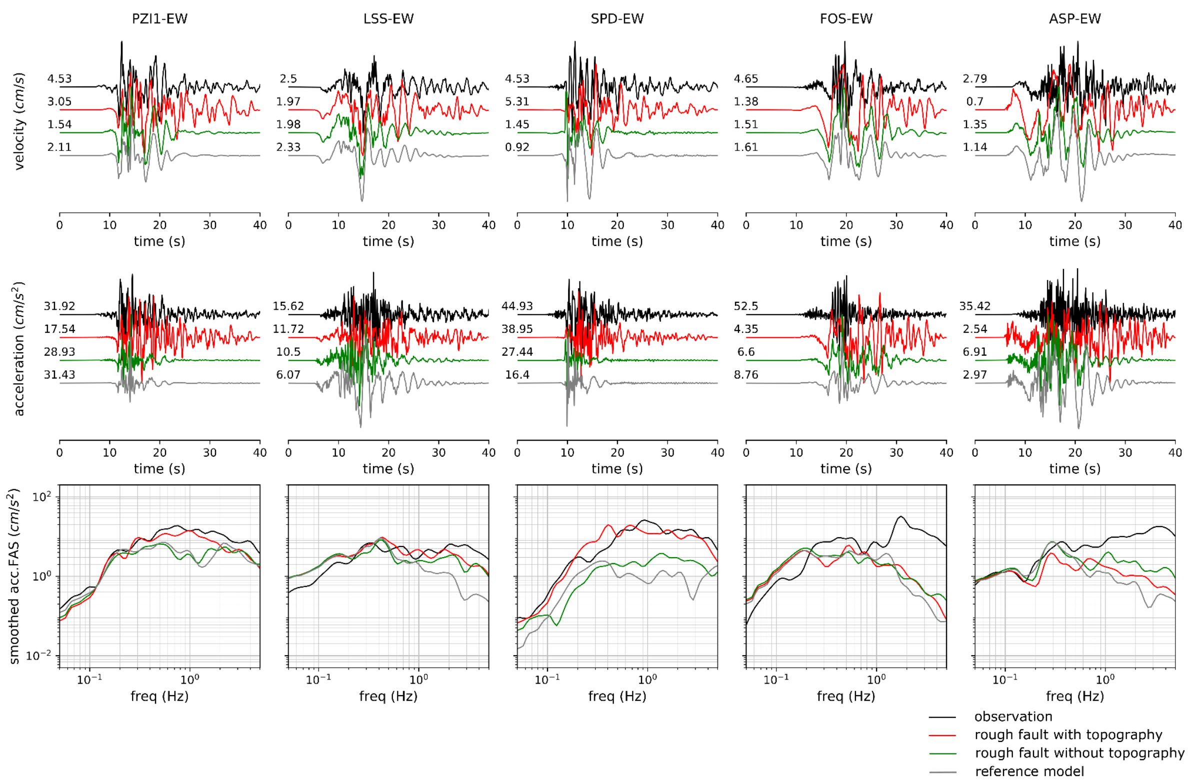

Figure 4. Broadband velocity and acceleration waveforms and Fourier amplitude spectra. (top, middle) Comparison of EW component of synthetic ground-velocity (top rows) and acceleration (middle rows) waveforms from the broadband rough fault model with topography (red), the broadband rough fault model without topography (green), and the reference model (grey) compared with observations (black) at five selected stations (see Figure 1). All waveforms are scaled by their maximum values, indicated on the left-hand side of each plot. (bottom) Smoothed (using the method of Konno & Ohmachi, 1998) Fourier amplitude spectra (FAS) of the velocity waveforms. The observed data is tapered with a 35 s cosine window.

AGU PUBLICATIONS

Geophysical Research Letters

Supporting Information for

Broadband dynamic rupture modeling with fractal fault roughness, frictional heterogeneity, viscoelasticity and topography: the 2016 Mw 6.2 Amatrice, Italy earthquake

T. Taufiqurrahman[1], A.-A. Gabriel[1], T. Ulrich[1], L. Valentová[2], F. Gallovič[2]

[1]Department of Earth and Environmental Sciences, Faculty of Geosciences, Ludwig Maximilian University, Munich, Germany

[2]Department of Geophysics, Faculty of Mathematics and Physics, Charles University, Prague, Czech Republic

Contents of this file

12. Figure S6-S12: Comparison of the observed and synthetic velocity, acceleration waveforms, and Fourier amplitude spectrums (FAS) of both the planar fault and the broadband rough fault model for EW and NS-components
13. Figure S13: Comparison of the observed, synthetic of the planar fault model with topography and without viscoelastic attenuation, and synthetic velocity waveforms of the planar fault model with topography and with viscoelastic attenuation
14. Figure S14: Histograms of Goodness-of-fit (GOF) between observation and velocity waveforms of the planar fault and the broadband rough fault model for all three-components
15. Figure S15: Comparison of Goodness-of-fit (GOF) between the planar fault and the broadband rough fault model for all three components for all stations
16. Figure S16: Model bias plot comparing between observation and velocity waveforms of the planar fault model, and the broadband rough fault model

Additional Supporting Information (Files uploaded separately)

1. Movie S1: Absolute slip rate (m/s) across the fault for the reference and the broadband rough fault models: https://drive.google.com/file/d/1TXFbNAshgfduapUGMWZWi413tgzwZNN5/view?usp=sharing
2. Movie S2: Top view of fault parallel (u) ground surface velocity for the reference model: https://drive.google.com/file/d/1qbwnd5iFs5R8AAA2by1Q3NGSrC-SkKcY/view?usp=sharing
3. Movie S3: Top view of fault normal (v) ground surface velocity for the reference model: https://drive.google.com/file/d/1I1yi9le_BusxM6ZGYCtYf4CQ0S0HluRQ/view?usp=sharing
4. Movie S4: Top view of vertical (w) ground surface velocity for the reference model: https://drive.google.com/file/d/1yAvXXEsGGwVRQKeOhJXG8J1o_jkwQAIf/view?usp=sharing
5. Movie S5: Top view of fault parallel (u) ground surface velocity for the broadband rough fault model with topography: https://drive.google.com/file/d/1xdlG5_KPVXe52AogYztJnBFoZcW9czAQ/view?usp=sharing
6. Movie S6: Top view of fault normal (v) ground surface velocity for the broadband rough fault model with topography: https://drive.google.com/file/d/1PSDfvSM5bS-WO-U_Ls0-wp-oHZC5JGJz/view?usp=sharing

2

7. Movie S7: Top view of vertical (w) ground surface velocity for the broadband rough fault model with topography: https://drive.google.com/file/d/1aIHHXBIBf9VNnDBJkhjZKWBqiavWCG8H/view?usp=sharing

Text S1. Numerical discretisation and resolution

Our high-resolution 3D dynamic rupture simulations are performed using the open-source software package SeisSol (https://github.com/SeisSol/SeisSol) resolving seismic wave excitation locally up to 10 Hz and ground motions up to at least 5 Hz within 50 km distance of the fault. SeisSol is based on the Arbitrary high-order DERivative Discontinuous Galerkin (ADER-DG) method (Dumbser & Käser, 2006; Pelties et al., 2012, 2014).

The dimensions of the model are 300 km x 300 km x 150 km (depth). We gradually increase the element size towards a maximum edge length of 10 km at the domain edges to reduce computational cost without sacrificing accuracy in the region of interest. This region is a highly resolved subdomain spanning 50 km x 50 km horizontally and 10 km in depth, centered at the hypocenter. There the high-order accurate element edge lengths range from 150 to 350 m, adapted to the 1D velocity model and requiring at least two elements resolving the shortest wavelengths (Käser et al., 2008), computed for a target frequency of 5 Hz.

We adapt the planar fault to adhere to band-limited fractal surface morphology characterized by wavelengths ranging from λ_{min}=200 m to λ_{max}=2 km. At least n=2 elements per wavelength λ_{min} are required to capture the complexity of the band-limited rough fault model without aliasing with SeisSol, which uses unstructured tetrahedral meshes. In this study, the rough fault is generated using the Fourier transform method. The rough fault can, therefore, be viewed as a weighted sum of sinusoids, which are here approximated by piece-wise bilinear functions due to SeiSol's geometrically linear triangles representing fault surfaces. We note that this leads to an artificial enhancement of the shorter wavelength content of the rough geometry.

For example, a 2-node approximation of a sine wave of wavelength λ can be decomposed into the sum of sinusoids of wavelength λ and its multiples λ/p. By using higher n, we decrease the artificial short-wavelengths content of wavelengths shorter than λ_{min} . The rough fault geometry then better resembles a band-limited fractal distribution. Low n (i.e., 2 to 4) are sufficient to capture the effects of fault roughness on earthquake dynamics and ground motions and also promote well-balanced numerics by limiting the number of elements with dynamic rupture boundaries. Even higher n would allow the discrete fault geometry to approach curvilinear approaches (e.g., Duru & Dunham, 2016) and for a better control of the amplitude spectrum of fault roughness at short wavelengths.

For our choice of n=4, the fault is discretized using 50 m sized elements, ensuring that the process zone size and thus rupture dynamics are sufficiently resolved everywhere on the fault (Day et al., 2005; Wollherr et al., 2018). We measure the minimum process zone size, the region behind the rupture front where the fault strength drops from its static to dynamic level, as being equal to 200 m. The resulting mesh has more than 80 million tetrahedral elements (Figure 1a) and is generated using Simmodeler (Simmetrix Inc., 2017). Simulating 40 s of a broadband Amatrice dynamic rupture earthquake scenario using SeisSol with fifth-order accuracy in space and time (i.e., basis functions of polynomial order p=4) and double precision requires 4 hours on 256 nodes of the SuperMUC-NG supercomputer.

Text S2. Empirical quantification of the 3D roughness drag

We empirically approximate the roughness drag ${\tau_{\mathrm{drag}}}^{\mathrm{3D}}$ (Equation 2) through systematic dynamic rupture simulations varying C, the minimum roughness wavelength λ_{min}, and the number of elements n resolving λ_{min}. We remind the reader that C is a dimensionless coefficient for empirical approximation of the 3D roughness drag. We find the preferred scenario for each parameterisation by comparing the space-time evolution of dynamically self-sustained rupture along the fault, seismic moment, peak seismic moment release, and timing of the peak seismic moment release to the reference model. We find that approximating C, as

$$C \approx m\ \lambda_{\mathrm{min}} + b\ , \qquad \text{(S1)}$$

i.e., a linear function with slope m = 0.001 and intercept b = 0.315(1 - 1 / n), allows us to recover broadband models matching the reference model for a range of broadband dynamic rupture models and discretizations (Figure S1a). Figure S1b shows analyzed and preferred values of intercept b for varying number of elements n per λ_{min}.

Text S3. Empirical quantification of the 3D roughness drag

We adapt the reference loading, which is prescribed as smoothly varying fault local initial tractions, to an equivalent globally defined Cartesian background stress allowing for geometry-induced small-scale traction heterogeneities. In this way, we can also account for the above quantified 3D roughness drag while preserving the smooth reference initial stress distribution. We build a heterogeneous stress tensor from τ_{dip}, τ_{strike}, and σ_{n} (see Section 2.2). The reference coordinate system of our model has the x-axis aligned with fault strike and the y-axis horizontal, pointing away from the hanging wall. We load the fault by an initial stress tensor (σ_{ij}) defined in a fault coordinate system (x,u,v) aligned with the planar reference model fault. v points up-dip, and u is oriented normally to the fault such that (x,u,v) forms a right-handed coordinate system. We set

4

$-\sigma_{uv} = \tau_{dip}$, $-\sigma_{xu} = -\sigma_{xv} = \tau_{drag}^{3D}$ to compensate for the 3D roughness drag effects on all initial shear stresses components, and $-\sigma_{xx} = -\sigma_{vv} = -\sigma_{uu} = \sigma_n$ (assuming compressive normal stresses being negative). This stress tensor is finally rotated by 45^o , the dip angle of the planar reference fault, with respect to the x-axis to the reference coordinate system. The resulting heterogeneous initial loading features roughness-induced small-scale fluctuations of the initial shear and normal tractions (Figure 2b), consisting of both releasing and restraining slopes, in which the fault is brought closer (resp. farther away) from failure (Fig S2a).

Due to the added τ_{drag}^{3D} term, the initial shear traction may exceed the initial fault strength locally. To prevent instantaneous failure across the fault, we limit τ_{dip} and τ_{strike} to be at least 0.5 MPa lower than fault strength everywhere on the fault except the nucleation area. Rupture is initiated in an area of negative strength excess of ~1 km radius located 16 km along-strike and 7 km down-dip (highlighted by a black line in Figure 2a,b). We empirically find that in the such modified rough fault model, 30% higher negative strength excess (τ_s-τ_0) of ~1.3 MPa is required to model the dynamically very sensitive weak nucleation from the reference model.

Text S4. Goodness of fit of broadband and reference ground motion

We quantify the fit between observations and synthetic ground-motions for all models (reference, broadband without topography, and broadband with topography) using Goodness-of-fit (GOF) metrics (Olsen & Mayhew, 2010). We compute the average GOF of 0.05–5 Hz bandpass filtered signals using the following metrics:

- Peak ground velocity (PGV)
- Peak ground displacement (PGD)
- Spectral Acceleration (SA) at periods 0.5-10 s
- Fourier amplitude spectra (FS)
- Energy duration (DUR)
- Cumulative energy (ENER)

We do not consider PGA because it is susceptible to site effects, which we do not account for in this study. Note that in our GOF computations, we exclude station RQT, for which no NS-component recording is available, and station CLF because of its strong broadband site-effect (class D).

Figure S14 shows the distribution of average GOF at all station components for the reference and both rough fault models. The histograms in Figure S14 show the prevalence of fairly good values (GOF 45-65) for both reference and rough fault models. The rough fault model with topography fits the observations generally better than the reference model and the rough fault model without topography for all components, with

5

an average GOF of 55, 65 and 55 for EW, NS and Z components, respectively. The best fit stations (GOF > 55 for all components) are PZI, LSS and TERO, located SE from the fault. Figure S15 details the average GOF for each station, component, and model. GOF values near or below 35 are observed at stations NRC and FEMA (EW components), stations NRC, ASP, and TRE (NS components), and station MNF (Z component).

We also calculate residuals r_j of spectral accelerations using the natural logarithm of the ratio of the observation O_j and synthetics S_j for each site j as a function of period T_i,

$$r_j(T_i) = \log[O_j(T_i) / S_j(T_i)] \qquad \text{(S3)}$$

Here, O_j and S_j are calculated as the geometric mean of the horizontal components. Mean model bias b for number of stations $N = 20$ is defined as

$$b(T_i) = 1/N\ \Sigma\ r_j(T_i) \qquad \text{(S4)}$$

with its standard deviation σ calculated as

$$\sigma(T_i) = [1/N\ \Sigma\ (r_j(T_i) - b(T_i))^2]^{½} \qquad \text{(S5)}$$

The model bias for the three tested models are shown in Fig. S15.

6

Table S1. Strong motion stations at which ground motion waveforms are compared in this study. All 20 stations are within a radius of 50 km from the Mw 6.2 Amatrice event epicenter.

Code	Station Name	Longitude (ºE)	Latitude (ºN)	Site Class* (EC8)
AMT	Amatrice	42.6325	13.2866	B
NRC	Norcia	42.7925	13.0964	B
MNF	Monte Fiegni (Fiastra)	43.0596	13.1844	A
TRL	Terminillo	42.4613	12.9323	B
ANT	Antrodoco	42.4182	13.0786	A
PZI1	Pizzoli	42.4356	13.3262	B
LSS	Leonessa	42.5582	12.9689	A
SPD	Sella Pedicate (Campotosto)	42.5151	13.371	B
FOS	Foligno Seggio	43.0146	12.8351	B
ASP	Ascoli Piceno	42.848	13.6479	B
TRE	Trevi	42.8765	12.7358	C
SPM	Spoleto (Monteluco)	42.7232	12.7512	A
FEMA	Monte Fema	42.9621	13.04976	A
TERO	Teramo	42.62279	13.60393	A
RM33	Pellescritta	42.50898	13.21452	B
RQT	Arquata del Tronto	42.813	13.311	A
SNO	Sarnano	43.0371	13.3041	B
CSC	Cascia	42.719	13.0122	B
MSC	Mascioni (Campotosto)	42.5268	13.3508	B
CLF	Colfiorito	43.03671	12.92043	D

*) the Engineering Strong-Motion database (https://esm.mi.ingv.it/, Luzi et al., 2016; Lanzano et al., 2021). Site classification according to EC8 (Eurocode 8, 2004).

Table S2. 1D Velocity model (Ameri et al., 2012) assumed in this study.

Depth (km)	Vp (km/s)	Vs (km/s)	ρ (g/cm^3)	Qp	Qs
0	3.16	1.70	2.50	200	100
1	4.83	2.60	2.84	400	200
2	5.76	3.10	2.94	400	200
5	6.51	3.50	3.15	400	200
27	7.00	3.80	3.26	600	300
42	7.80	4.20	3.50	800	400

 8

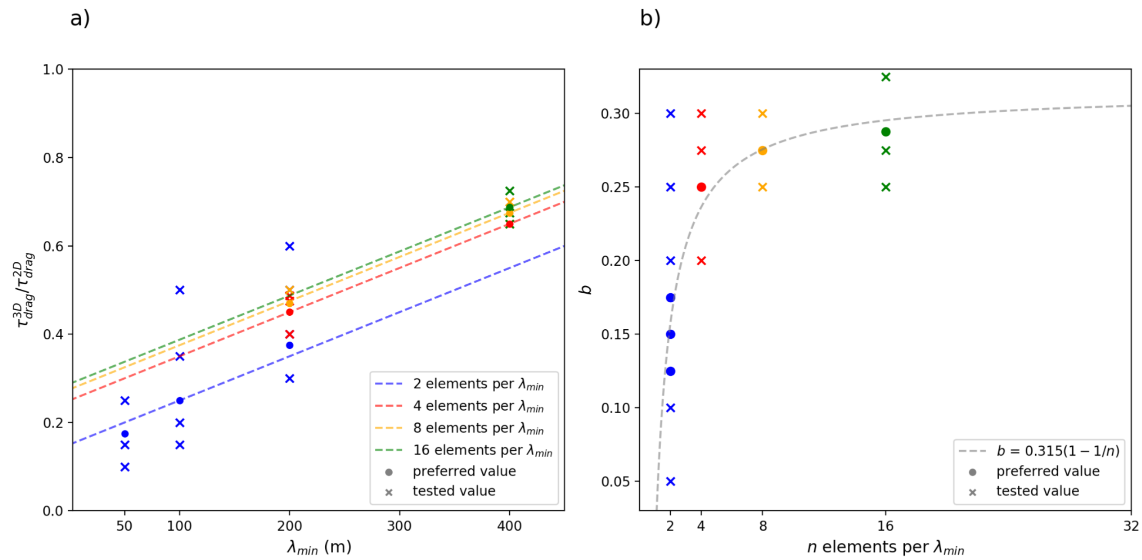

Figure S1. (a) Tested and preferred values of coefficient C (Eq. 2), relating $\tau_{\mathrm{drag}}{}^{3\mathrm{D}}$ to $\tau_{\mathrm{drag}}{}^{2\mathrm{D}}$ (Eq. 1), for varying minimum roughness wavelength λ_{min}. The preferred values of C (shown by full circles) are identified by comparing the moment rate release of the rough fault model to the reference model (b) Tested and preferred values of intercept parameter b (Eq. S1) for varying number of elements n per λ_{min}. The dashed line corresponds to the fitted function of b.

9

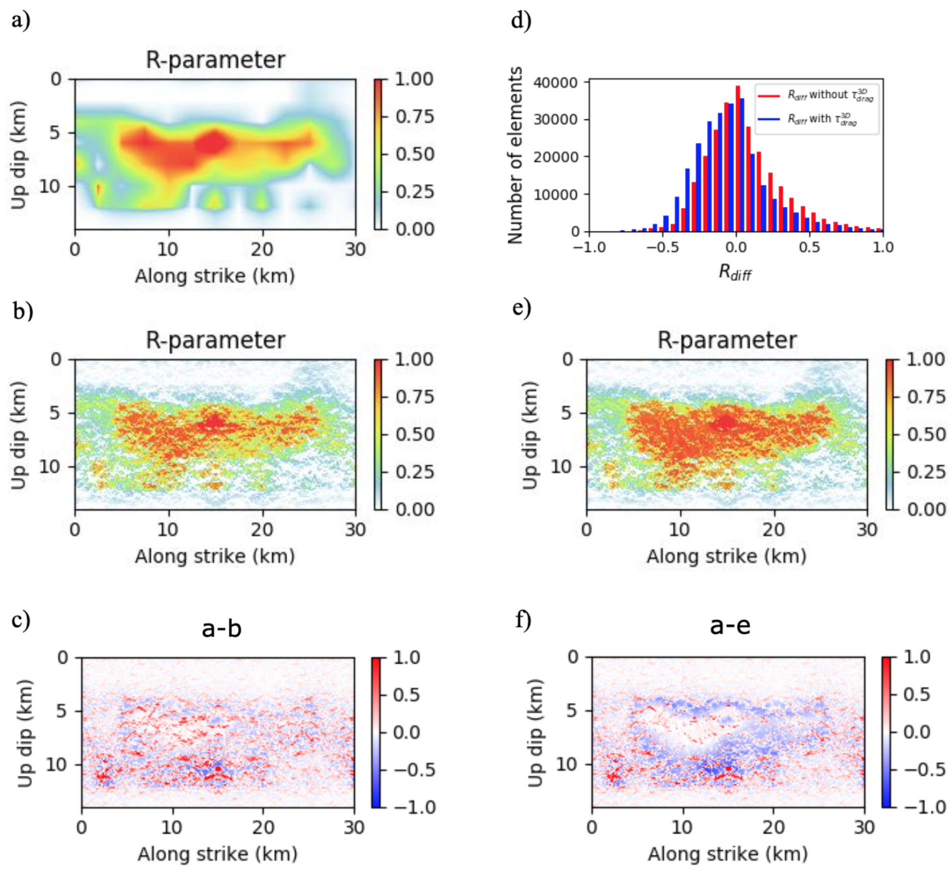

Figure S2. Comparison of the relative prestress ratio *R* for the planar reference model and the rough fault broadband model with and without roughness drag correction. We define the relative prestress ratio *R* following Aochi & Madariaga (2003) as the ratio of the potential stress drop $\Delta\tau$ to the full breakdown strength drop $\Delta\tau_b$, $R = \Delta\tau / \Delta\tau_b = (\tau_0 - \mu_d\sigma_n)/ ((\mu_s - \mu_d)\sigma_n)$. *R*=1 indicates a critically stressed fault. (a) *R* for the reference model, the broadband model (b) without and (e) with $\tau_{drag}{}^{3D}$; (c) difference of the *R*-parameter between (a) and (b), (f) difference of the *R*-parameter between (a) and (e); and (d) histogram of (c) and (f).

10

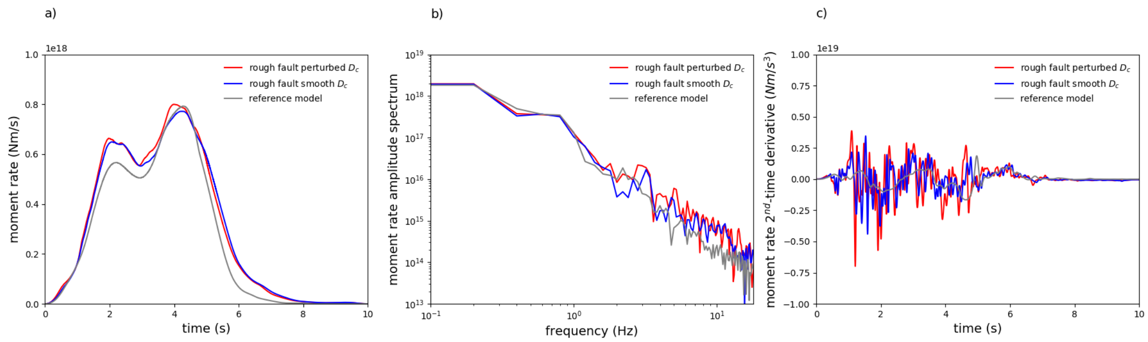

Figure S3. (a) Moment rate release, (b) moment rate spectrum, (c) the 2nd time derivative of the moment rate release. Grey curves correspond to the reference model. Red and blue curves correspond to the broadband rough fault model with and without D_c perturbations, respectively.

11

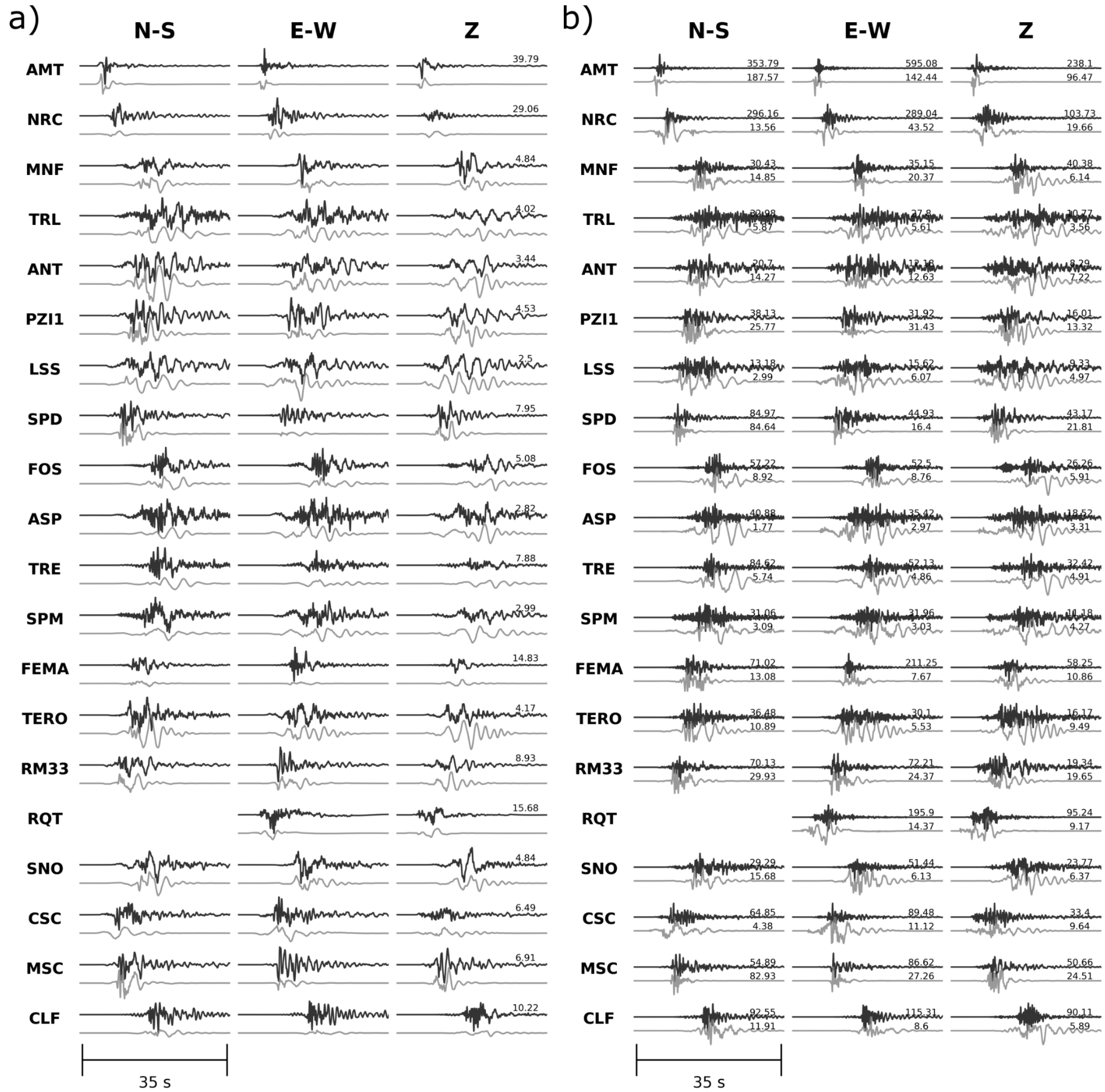

Figure S4. Comparison of observed (black) and simulated (grey) broadband three-component (NS, EW, and Z) of (a) ground-velocity (in cm/s) and (b) acceleration (in cm/s2) waveforms at 20 selected stations (Figure 1). Synthetics are from the reference dynamic rupture scenario based on a planar fault. Both observed and synthetic velocity waveforms are scaled by the maximum value of the observed records at each station, indicated on the right-hand side of each plot, while acceleration waveforms are scaled component-wise. Observed and synthetic waveforms are band-pass filtered between 0.05 and 5 Hz.

12

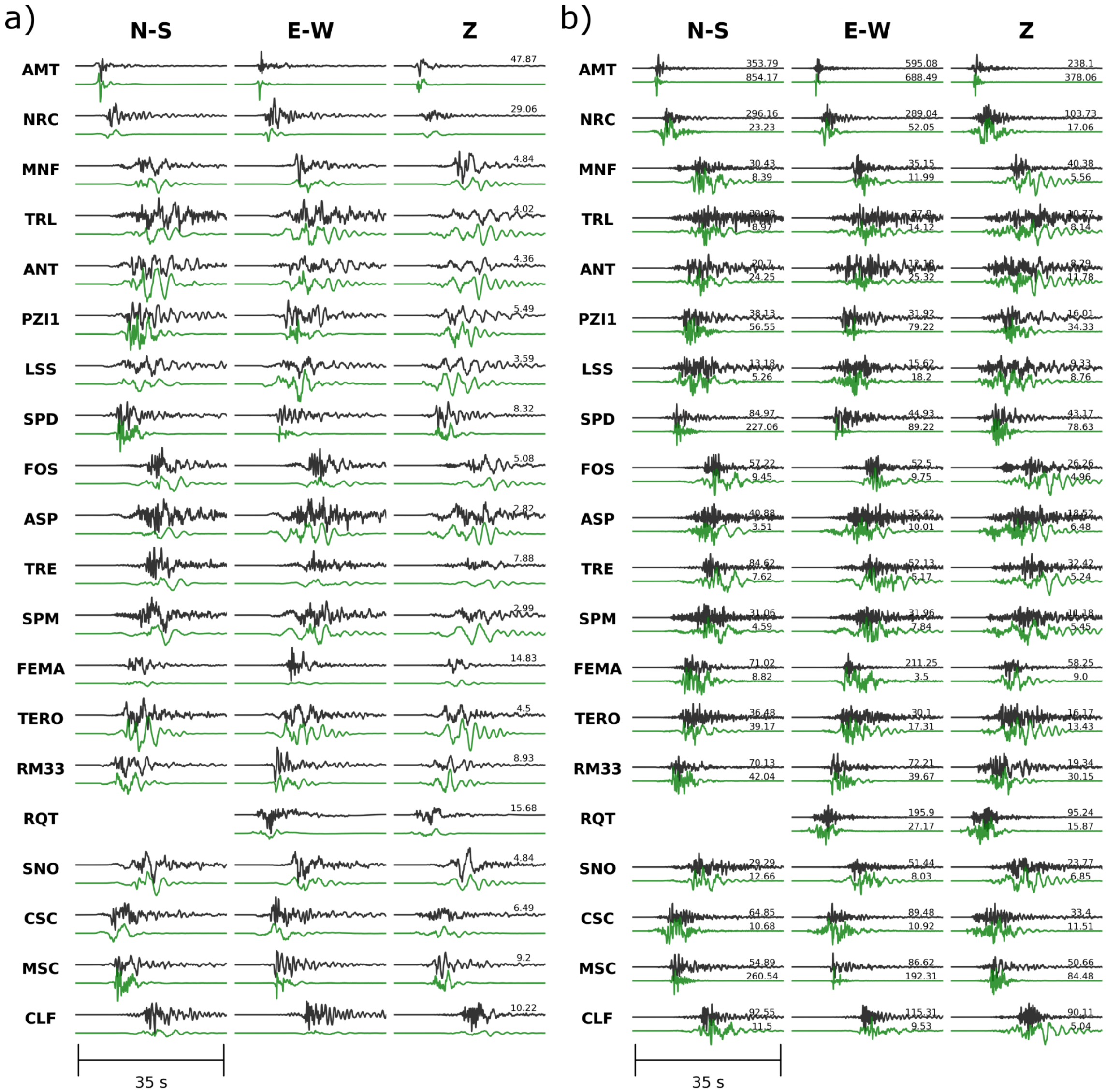

Figure S5. Comparison of observed (black) and simulated (green) broadband three-component (NS, EW, and Z) of (a) ground-velocity (in cm/s) and (b) acceleration (in cm/s2) waveforms at 20 selected stations (Figure 1). Synthetics are from the rough fault dynamic rupture scenario without topography. Both observed and synthetic velocity waveforms are scaled by the maximum value of the observed records at each station, indicated on the right-hand side of each plot, while acceleration waveforms are scaled component-wise. Observed and synthetic waveforms are band-pass filtered between 0.05 and 5 Hz.

13

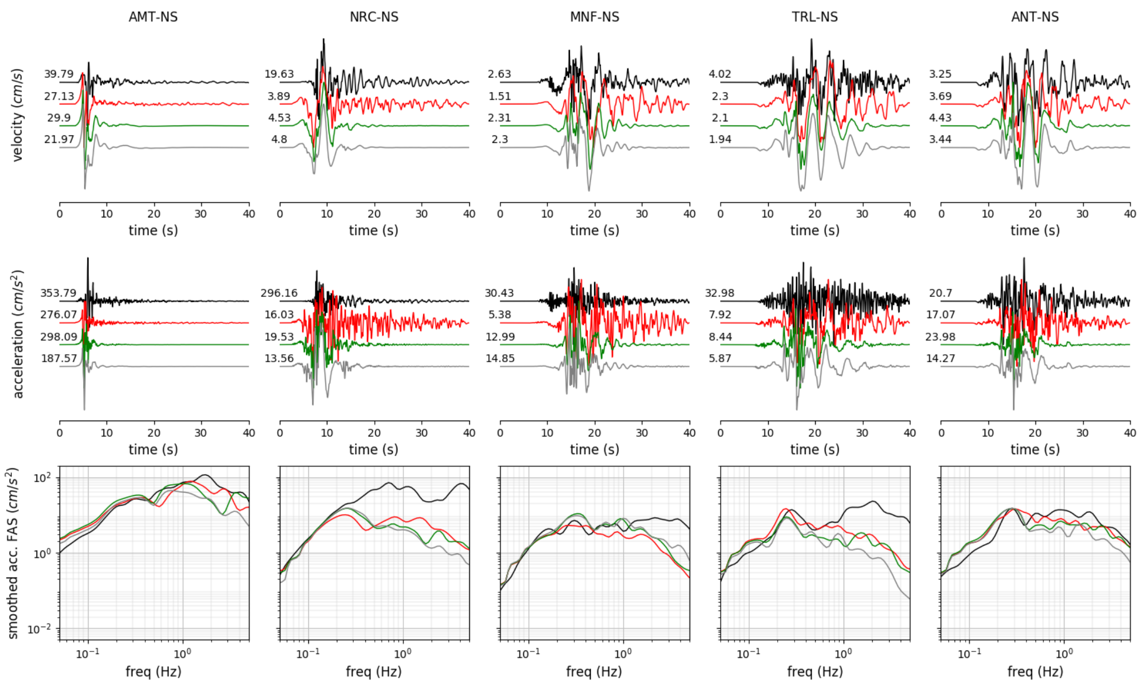

Figure S6. Effect of rough fault and topography on the velocity and acceleration waveforms and on the Fourier amplitude spectra. (top, middle) Comparison of synthetic ground-velocity (top rows) and acceleration (middle rows) waveforms from the broadband rough fault model with topography (red), the broadband rough fault model without topography (green), and the reference model (grey) compared with observations (black). NS component at five selected stations (see Figure 1). All waveforms are scaled by their maximum values, indicated on the left-hand side of each plot. (bottom) Smoothed (using the Konno & Ohmachi (1998) method) Fourier amplitude spectra (FAS) of the velocity waveforms.

 14

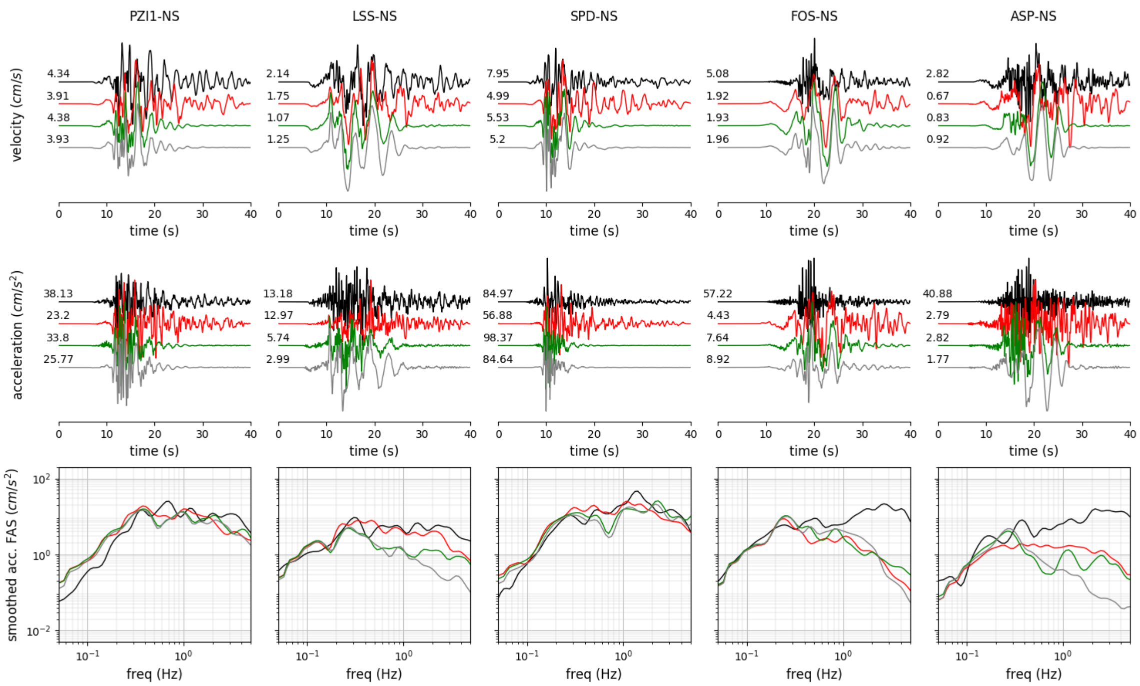

244 **Figure S7.** Same as Figure S4 for stations PZI, LSS, SPD, FOS, and ASP.

15

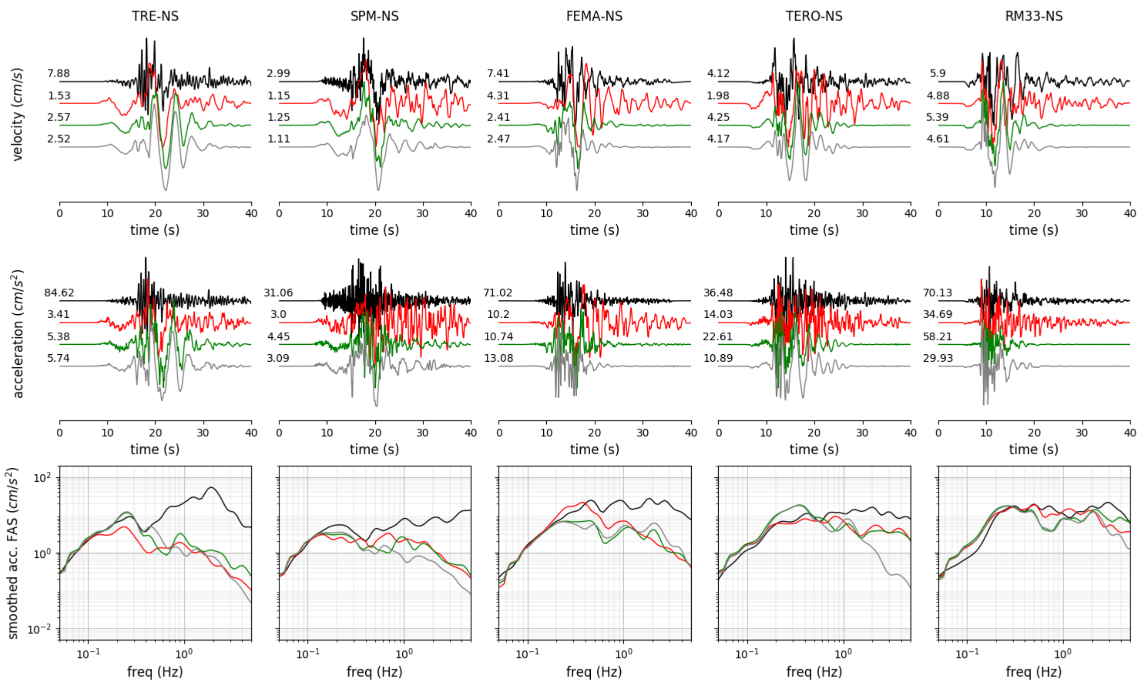

Figure S8. Same as Figure S4 for stations TRE, SPM, FEMA, TERO, and RM33.

16

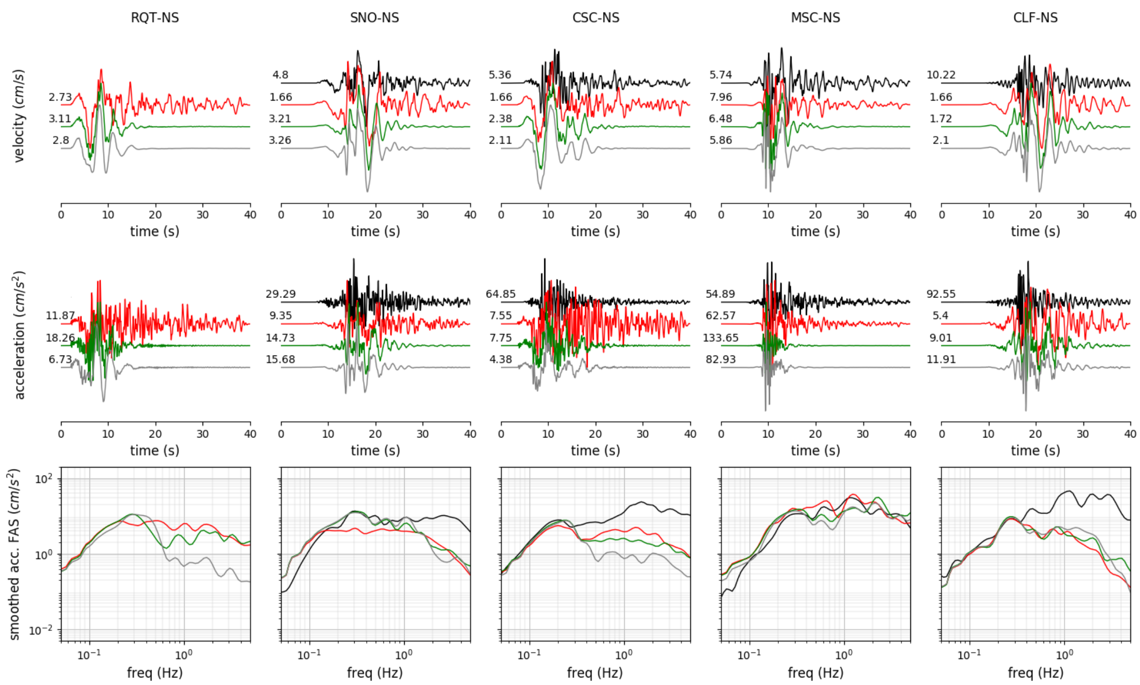

246 **Figure S9.** Same as Figure S4 for stations RQT, SNO, CSC, MSC, and CLF.

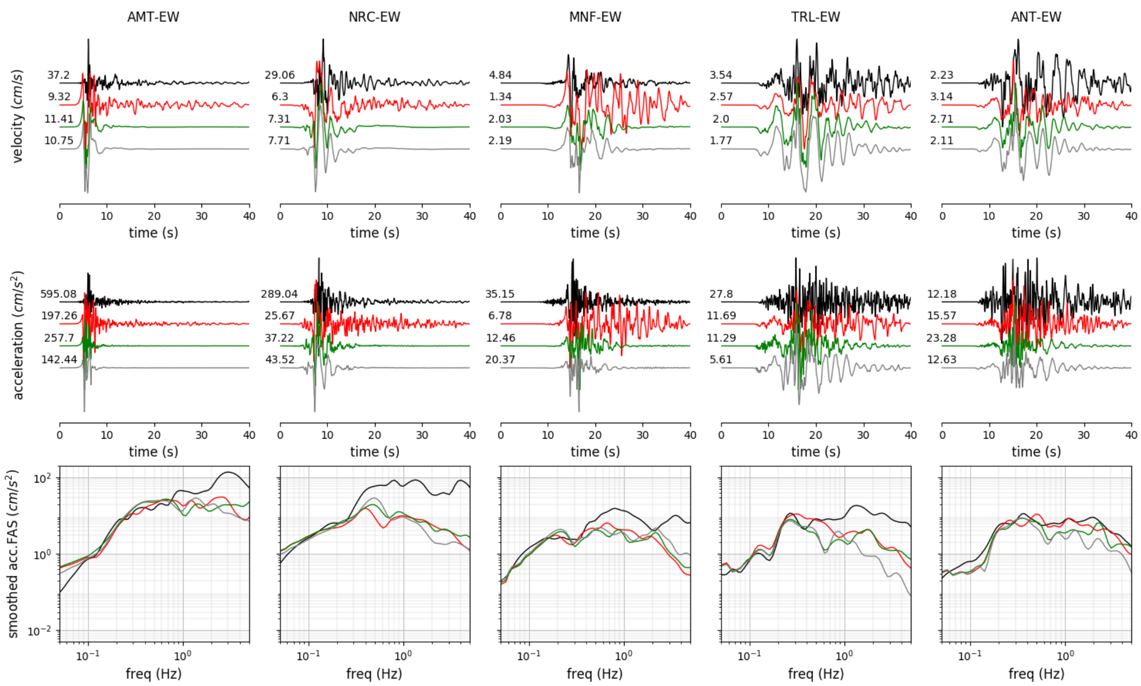

Figure S10. Effect of rough fault and topography on the velocity and acceleration waveforms and on the Fourier amplitude spectra. (top, middle) Comparison of synthetic ground-velocity (top rows) and acceleration (middle rows) waveforms from the broadband rough fault model with topography (red), the broadband rough fault model without topography (green), and the reference model (grey) compared with observations (black). EW component at five selected stations (see Figure 1). All waveforms are scaled by their maximum values, indicated on the left-hand side of each plot. (bottom) Smoothed (using the Konno & Ohmachi (1998) method) Fourier amplitude spectra (FAS) of the velocity waveforms.

 18

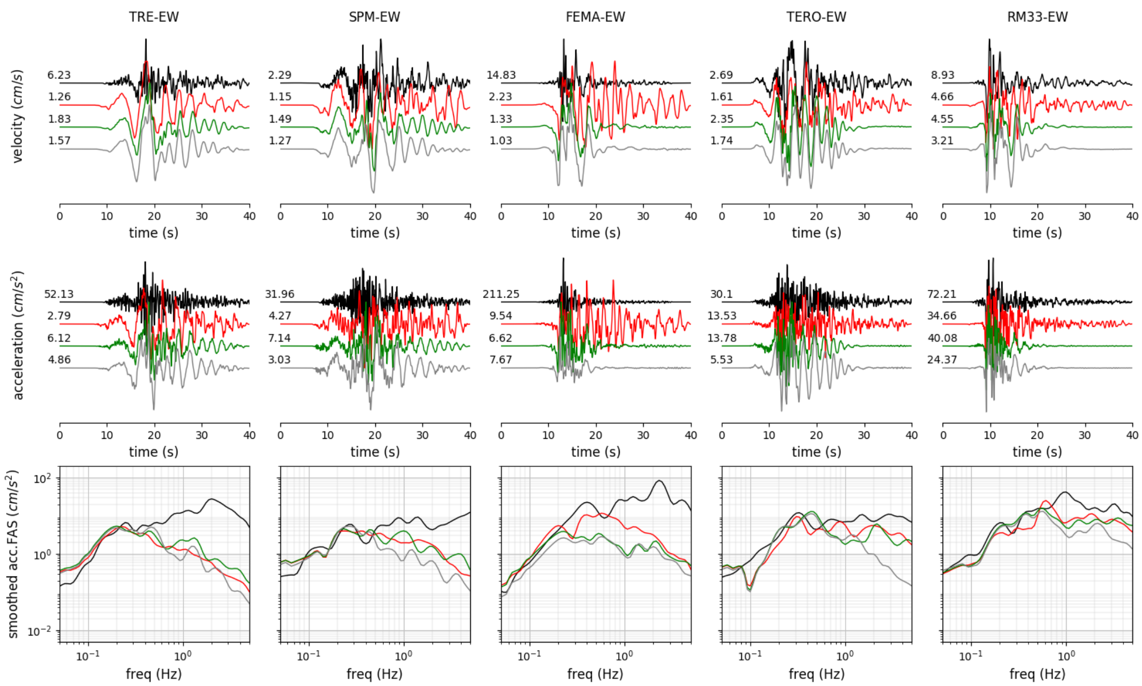

Figure S11. Same as Figure S8 for stations TRE, SPM, FEMA, TERO, and RM33.

19

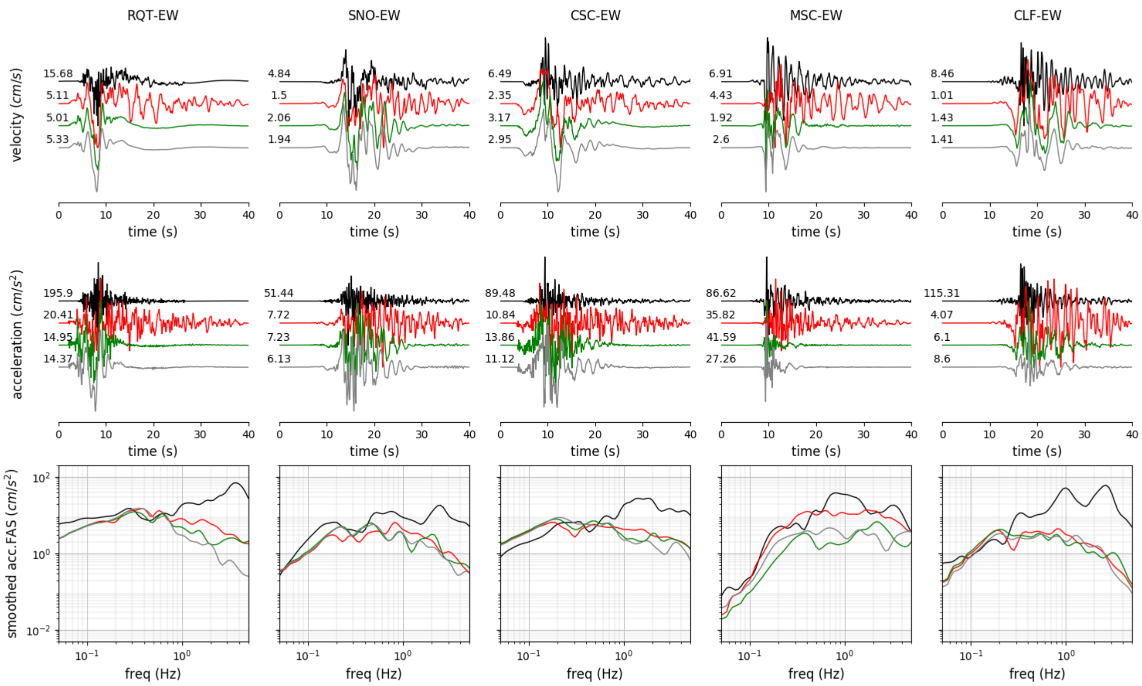

257 **Figure S12.** Same as Figure S8 for stations RQT, SNO, CSC, MSC, and CLF.

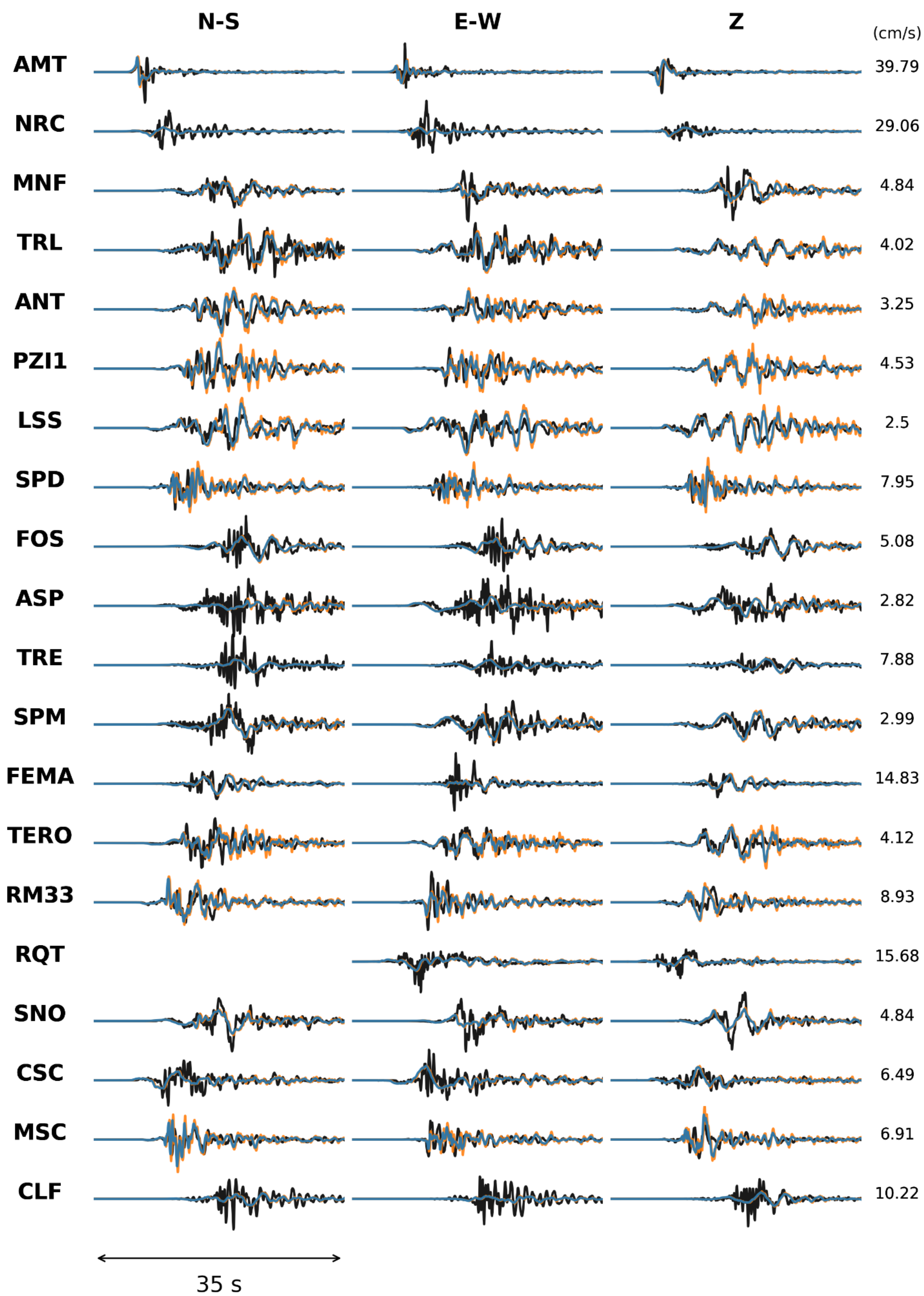

Figure S13. Comparison of observed (black) and simulated ground velocities for a planar fault model with topography with (cyan) and without (orange) viscoelastic attenuation at 20 selected stations (Figure 1). All observed and synthetic velocity waveforms are scaled by the maximum value of the observed records at each station, indicated in cm/s on the right-hand side of each plot. Observed and synthetic waveforms are band-pass filtered between 0.05 and 5 Hz.

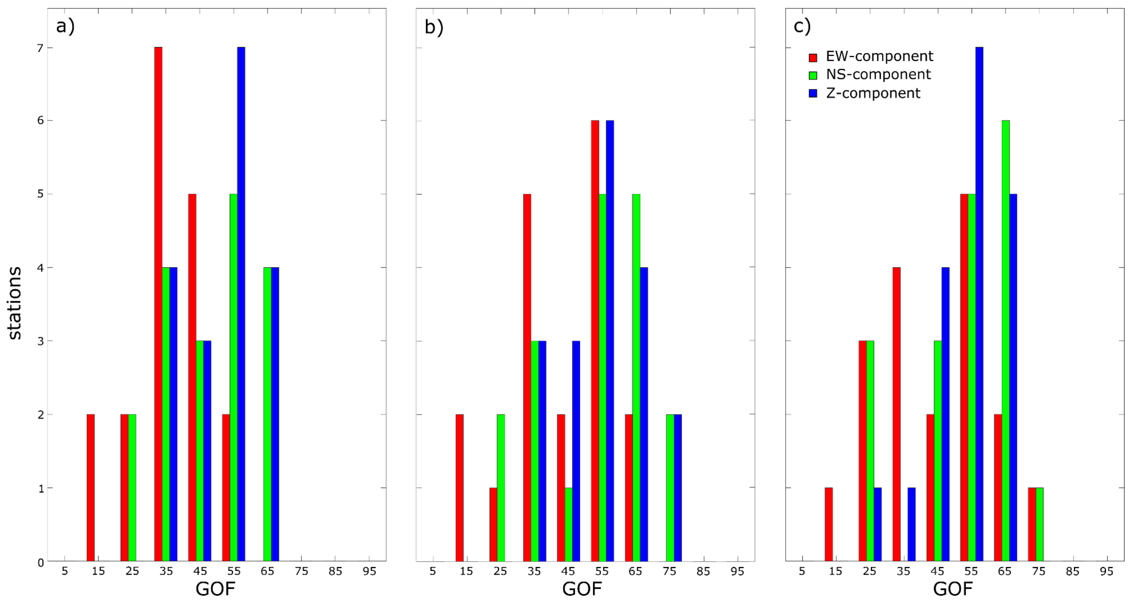

Figure S14. Distribution of average Goodness-of-Fit (GOF) for each component (color coded) for (a) the reference model, (b) the broadband rough fault model without topography, and (c) the broadband rough fault model with topography.

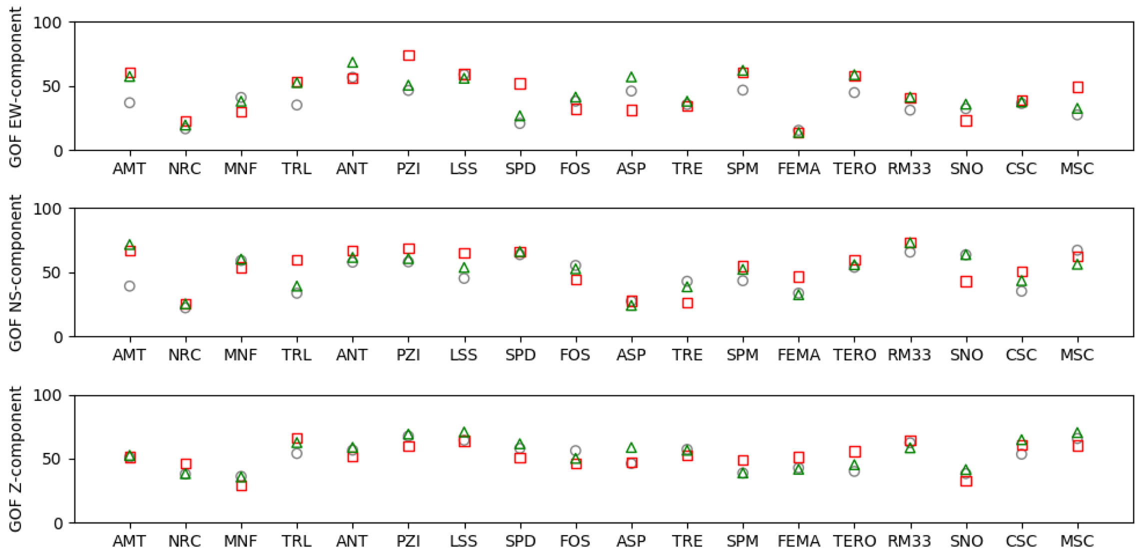

Figure S15. Average Goodness-of-Fit (GOF) for each station and component, for the reference (grey circles), the broadband rough fault model without topography (green triangles), and the broadband rough fault model with topography (red squares).

23

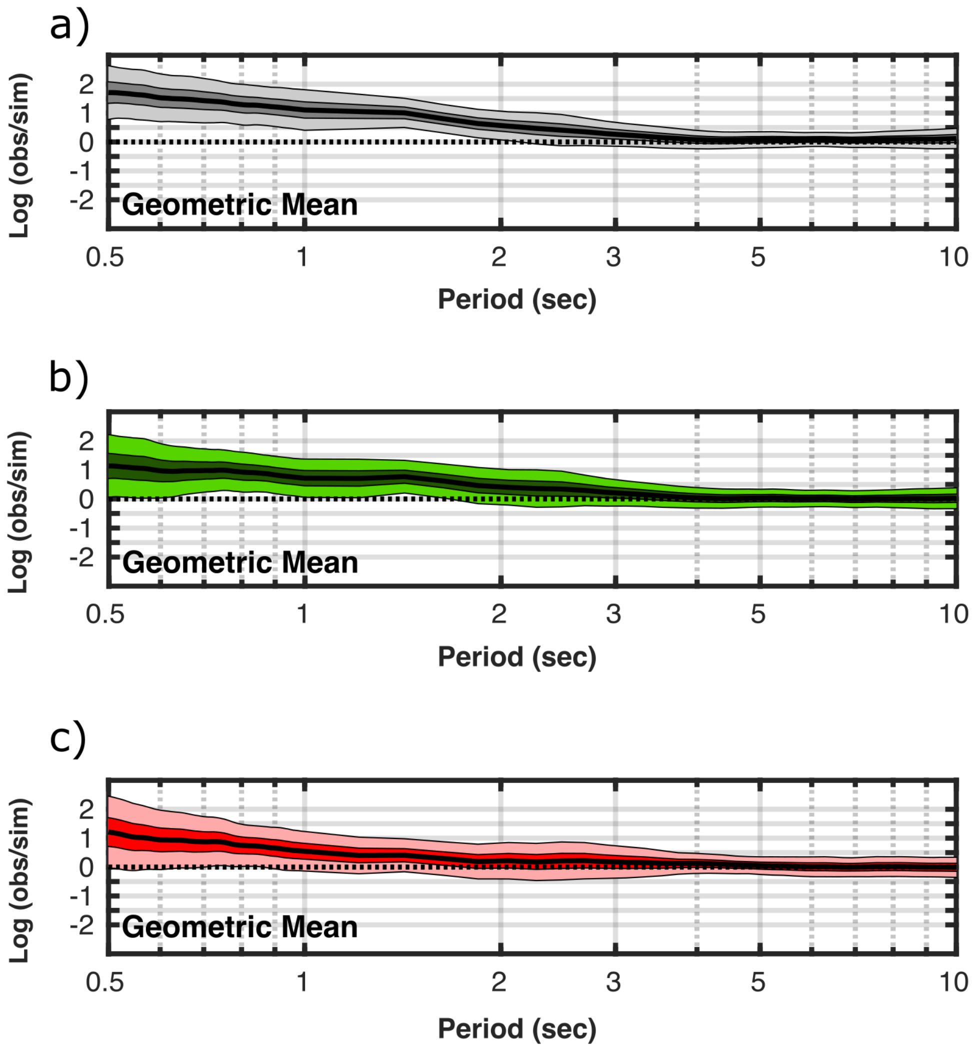

Figure S16. The model bias (dashed lines) and standard deviation (solid lines) of residuals between observed SA values in the 0.5-10 s period range, averaged over 20 stations and synthetics of (a) reference model, (b) broadband rough fault model without topography, and (c) broadband rough fault model with topography. The bold black line is the median value, the filled area is the 90% confidence interval and the pale filled area is the one-sigma range.

24